UNIVERSITY OF GRONINGEN
MASTER THESIS
07/2020



rijksuniversiteit
groningen

# Cold Gas Accretion in a Magnetised Circum-Galactic Medium

RICHARD KOOIJ

Supervised by
Prof. Dr. FILIPPO FRATERNALI
&
Dr. ASGER GRØNNOW

# Abstract

Observations show the presence of "cold" ($\sim 10^4$ K) gas around galaxies that is often in- or out-flowing at speeds on the order of 100 km/s. This cold gas co-exists with hot ($\sim 10^6$ K) galactic halos creating a complex, multi-phase circum-galactic medium. This circumgalactic medium is likely the source of gas accretion onto disc galaxies and thus the reservoir for star formation. Studying the interactions of cold gas with a hot galactic halo is thus vital to further understand galaxy formation and evolution.

These processes are typically investigated using hydrodynamical simulations of clouds moving through a hot medium (also called cloud-wind simulations). Simulations of this kind that include all relevant physics, specifically radiative cooling, magnetic fields, and thermal conduction have only recently been performed, due to their complexity. In particular, thermal conduction in the presence of a magnetic field is highly anisotropic, being strongly suppressed in the direction perpendicular to the magnetic field lines. In order to simplify the calculations, a common approach is to use a simple prescription to model the suppressed thermal conduction heat flux by assuming that thermal conduction is isotropic like in the classical Spitzer theory but at a certain efficiency $f$ lower than unity. Typical values used for $f$ are in the range $\sim 0.001 - 0.2$ of the Spitzer value, but this value is largely unconstrained in the context of galactic gas accretion.

In this work we investigate the effects of thermal conduction by comparing the evolution of 3D hydrodynamical (HD) simulations using artificially suppressed isotropic thermal conduction with $f$, against 3D magneto-hydrodynamical (MHD) simulations with (true) anisotropic thermal conduction. We explore different strengths and orientations of the magnetic field, different densities and metallicities of the media and different relative velocities between the cloud and the hot gas. Our main diagnostic is the evolution of the amount of cold gas as a function of time in the simulation domain. We found that in almost every HD and MHD run, the amount of cold gas increases with time, indicating that hot gas condensation is an important phenomenon that can contribute to gas accretion onto galaxies. When the magnetic field is oriented transverse to the cloud velocity, a configuration that we consider realistic in most situations, we find that $f$ is in the range $0.03 - 0.15$. The efficiency of thermal conduction is thus always highly suppressed, but the effect of thermal conduction in the cloud evolution is generally not negligible.

# Contents

# Chapter 1

# Introduction

In addition to the interstellar medium (ISM), star-forming galaxies such as the present-day Milky Way are expected to have a lower density, extensive gaseous halo surrounding them. This halo is very massive, multi-phase and is defined as the circum-galactic medium (CGM). Common nomenclature that will be used in this thesis is how we refer to the different temperature phases in the CGM: we define the "cold" phase as gas at $T \sim 10^4$ K, the "warm" phase at $T \sim 10^5$ K, and the "hot" phase at $T \sim 10^6$ K. In this thesis I aim to increase our knowledge on the interactions between cold and hot gas in the CGM, and in particular on the effects of thermal conduction in the presence of magnetic fields. To achieve this I have performed novel 3D magneto-hydrodynamical simulations with fully anisotropic thermal conduction and radiative cooling of a cold cloud moving through the hot CGM.

In this chapter I will introduce the constituents of the CGM and highlight their importance for the evolution of galaxies. After this I will introduce how the interactions in the CGM are studied numerically, and give a brief overview of the physics that is expected to be dominant in these systems.

## 1.1 The Circum-galactic Medium

Observations have shown that the CGM of galaxies is a complex, multi-phase structure where cold ($T \sim 10^4$ K) gas clouds co-exist with an ionised, hot ($T \sim 10^6$ K) diffuse halo (Putman et al., 2012; Tumlinson et al., 2017). The CGM is thought to be maintained by flows of gas from and towards galaxies, which cause a strong interplay between the hot and cold gas phases. The properties of these hot and cold phases and how they interact with each other are poorly understood. Nevertheless, these interactions are expected to be very important for the process of gas accretion onto galaxies, which makes the CGM vital to study to further our understanding of galaxy evolution.

### 1.1.1 Hot gas phase

The idea of a hot halo around the Milky Way arose as a hypothesis by Spitzer (1956) to provide pressure support to observed gas clouds away from the Galactic disc, the so-called High Velocity Clouds (HVCs, Muller et al., 1963). The existence of such hot halos around galaxies was later theoretically predicted as gas accreted from the intergalactic medium (IGM), that is shock-heated to the virial temperature (White & Rees, 1978; White & Frenk,
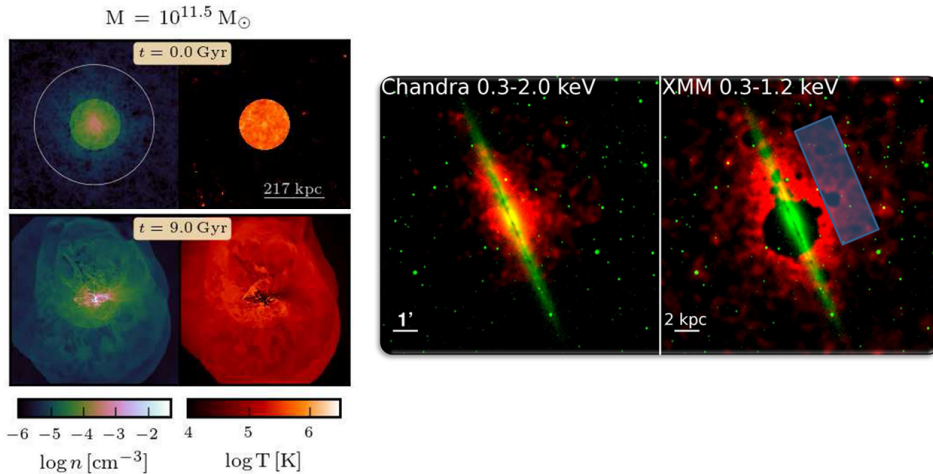
*Figure 1.1: On the left, we show two density (left) and temperature (right) snapshots of a cosmological galaxy simulation with stellar feedback, which shows that a low density, hot, extensive halo can form and be sustained over cosmic times (Figure adapted from Fielding et al., 2017). On the right panels, we show Chandra and XMM-Newton observations of X-ray emission (in orange) around NGC 891, overlaid on an optical image (Hodges-Kluck & Bregman, 2014). Both images show diffuse emission extending significantly beyond the stellar disc.*

1991; Birnboim & Dekel, 2003). Hot halos are furthermore consistently formed in Lambda Cold Dark Matter (ΛCDM) cosmological simulations (Fumagalli et al., 2014; Fielding et al., 2017, see Figure 1.1, left). They are expected to extend to the virial radius ($\sim 250$ kpc for the Milky Way, Fukugita & Peebles, 2006), and contain a significant fraction of the baryonic mass of galaxies (Dai et al., 2012; Gatto et al., 2013; Bregman et al., 2018), which might be the source of gas for the prolonged star formation rates observed in typical galactic discs (e.g. Bauermeister et al., 2010).

The hot phase of the CGM is difficult to detect directly, due to its low X-ray surface brightness (e.g. Bregman, 2007). However, an X-ray excess around some massive early-type galaxies is known to exist for a long time (e.g. Forman et al., 1979, 1985). Recently, using the new generation of X-ray telescopes they have also been detected around late-type galaxies (Anderson & Bregman, 2011; Humphrey et al., 2011; Yamasaki et al., 2009; Bogdán et al., 2012; Hodges-Kluck & Bregman, 2014; Anderson et al., 2016, see Figure 1.1, right). Evidence in support of a hot galactic halo also comes from absorption line studies towards distant active galactic nuclei (AGN) (e.g. Miller & Bregman, 2013; Stocke et al., 2013). Additional evidence is obtained indirectly from the head-tail structure that is observed in some HVCs (e.g. Brüns et al., 2000; Putman et al., 2011), or from dwarf satellite galaxies that are devoid of gas, which indicates ram-pressure stripping by a diffuse medium (e.g. Grcevich & Putman, 2009).

### 1.1.2 Cold gas phase

The cold gas phase in the CGM of the Milky Way is typically detected using H I 21-cm emission, and has revealed a large population of extra-planar HVCs (e.g. Muller et al., 1963; Wakker & van Woerden, 1991, 1997; Tufte et al., 1998; Braun & Burton, 2000; Wakker, 2001; Wakker et al., 2007), see e.g. the left panel of Figure 1.2. These clouds are char-
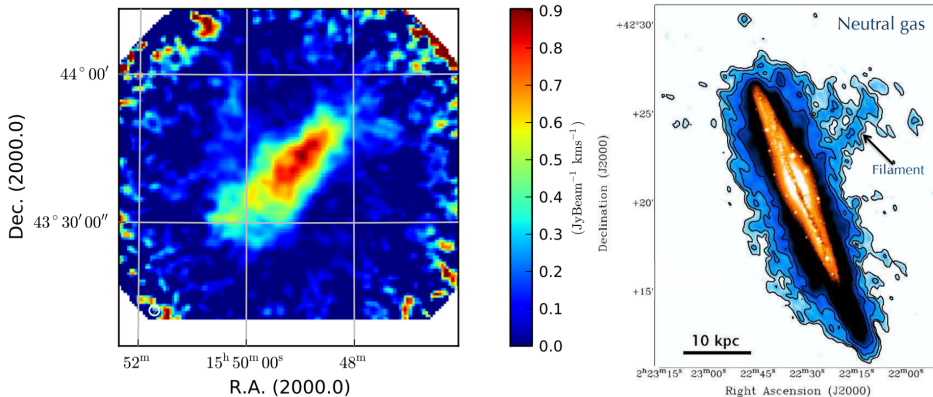
*Figure 1.2: On the left we show an H I emission map of combined Westerbork Synthesis Radio Telescope (WSRT) and 100-meter Heffelsberg telescope data of a "compact" (as defined by Braun & Burton, 2000) high velocity cloud around the Milky Way (Faridani et al., 2014). On the right we show an H I emission map around NGC 891 obtained with WSRT (Oosterloo et al., 2007), which is overlaid on an optical image in orange. The neutral gas clearly extends far beyond the stellar disc.*

acterised by velocities of the order of 100 km/s with respect to the local standard of rest that are inconsistent with the rotation of the Galactic disc. A subset of these gas clouds are characterised with lower ($< 90$ km/s) velocities with respect to the local standard of rest and are called Intermediate Velocity Clouds (IVCs). It was found by Wakker (2001) that HVCs are typically metal-poor, while IVCs have metallicities close to solar. This difference hints at different origins: accretion for the HVCs and feedback for the IVCs (see Section 1.1.3).

Cold gas in external galaxies is also found in extended regions outside the stellar disc. This extraplanar neutral gas is for example seen in H I emission around NGC 891 (e.g. Oosterloo et al., 2007, see Figure 1.2, right), and typically contains an H I mass of the order of $\sim 10\%$ of the H I mass of the disc (e.g. Table 1 in Fraternali, 2017). More commonly, observational evidence of cold gas in external galaxies is presented through neutral hydrogen absorption lines (e.g. Lyman-$\alpha$) along sightlines to distant AGNs (e.g. Prochaska & Hennawi, 2008; Hennawi et al., 2015; Lau et al., 2016), and other low temperature absorption lines such as C II, Si II, Mg II (Werk et al., 2013; Crighton et al., 2013, 2015).

A warm ($\sim 10^5$ K) phase is also found using UV absorption of ionisation states including C IV, Si IV, and O VI in both the Milky Way (e.g. Sembach et al., 2003; Richter et al., 2017), and in external galaxies (e.g. Tumlinson et al., 2011; Stocke et al., 2013; Werk et al., 2014; Lehner et al., 2015; Werk et al., 2016; Zheng et al., 2017; Qu et al., 2019). While the origin of this intermediate temperature gas in the CGM is not entirely clear, its presence could be explained by the interactions between cold clouds moving through a hot halo (see e.g. Marasco et al., 2013; Fraternali et al., 2013). However, most hydrodynamical simulations do not reproduce this phase (e.g. Marinacci et al., 2010). The addition of thermal conduction to these simulations might help to keep gas at these intermediate temperatures (Armillotta et al., 2017).

The observational evidence presented confirms the existence of cold gas moving through the halo regions of galaxies, and indicates that the CGM must be a highly dynamic environment.
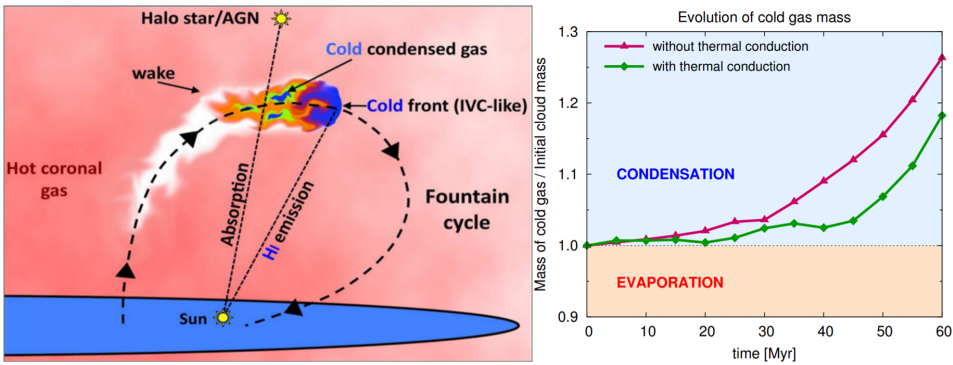
*Figure 1.3: A sketch (upper left) showing the galactic fountain model as described by Fraternali et al. (2013). A gas cloud is ejected by supernova feedback and interacts with the hot halo, until it ultimately falls back onto the disc after having caused the condensation (cooling) of a fraction of the halo gas. On the right, we show the evolution of the cold gas mass in 2D hydrodynamical simulations including radiative cooling and thermal conduction of an IVC moving through the CGM of a Milky Way-like galaxy (Armillotta et al., 2016). The mass of cold gas in the simulations increases by $\approx 20\%$ over 60 Myrs.*

### 1.1.3 Gas flows in the CGM

The dynamics of the CGM is complicated and is driven by several processes. The expected main contributors are hot mode accretion, which consists of large scale inflow from the IGM, cold mode accretion, which consists of inflow of cold material by e.g. cold filamentary streams (e.g. van de Voort et al., 2012), and feedback from inside the galaxy itself. Gas in and around galaxies is continuously heated and ejected by feedback mechanisms from a variety of sources such as active galactic nuclei (AGN) (e.g. Antonuccio-Delogu & Silk, 2010), and supernovae (e.g. Martin, 1999; Mac Low & Klessen, 2004; Li et al., 2017). The origin of metal-rich IVCs is expected to be associated with supernovae. It is thought that supernovae create hot, ionised super-bubbles that eject gas clouds into the halo regions at velocities on the order of 100 km/s (Mac Low et al., 1989). The ejected gas consists of metal-rich disc material and is likely warm ($\sim 10^5$ K, Houck & Bregman, 1990). As it moves out of the disc it is slowed down by drag forces and ultimately falls back onto the disc, in a continuous circulation process called the galactic fountain (Shapiro & Field, 1976; Fraternali & Binney, 2006), see e.g. Figure 1.3. The metal-rich gas from the disc interacts with the metal-poor halo, and gas is stripped from the cloud primarily by Kelvin-Helmholtz instability (KH, Helmholtz, 1868; Kelvin, 1871) at the interface between cloud and hot halo. If the stripped metal-rich gas mixes efficiently with the halo gas, it can drastically reduce the cooling time of the latter (see e.g. Marinacci et al., 2010; Fraternali et al., 2015). The net effect is thus that ejected gas clouds can trigger the condensation of metal-poor material from the halo, generally referred to as supernova-driven accretion (Fraternali & Binney, 2008). It is argued that this process can provide the required cold gas to justify the observed star formation rates in galaxies (Fraternali & Binney, 2008; Marasco et al., 2012; Fraternali, 2017).

### 1.1.4 The magnetic field in the CGM

Evidence for magnetic fields in galaxies was first found by Brown & Hazard (1951) with radio observations of the Andromeda galaxy. More than a decade later it was first detected in

the Milky Way using the Faraday rotation measure (Westerhout et al., 1962; Wielebinski & Shakeshaft, 1962; Berkhuijsen & Brouw, 1963). Current knowledge suggests that both the ISM and the CGM of spiral galaxies are magnetised. While much of the precise structure and magnitudes remain unknown, Faraday rotation measures have shown that the spiral arms of the Milky Way have amplified magnetic fields (Beck, 2003; Brown et al., 2007). It was later shown that the Galactic magnetic field can indeed be of the order of tens of $\mu$G in the spiral arms and the bulge region, while having an average value of $\approx 3\mu$G (Beck, 2009, 2015).

Magnetic fields are also observed outside the discs of spiral galaxies, in the halo region (e.g. Ekers & Sancisi, 1977; Sancisi & Allen, 1979; Irwin et al., 2012). It remains however very hard to infer the magnetic field orientation and strength in the halo of the Milky Way. Based on combined Wilkinson Microwave Anisotropy Probe 5 (WMAP5, Komatsu et al., 2009) polarisation data and Faraday rotation measures, it is shown by Jansson et al. (2009) that most Galactic field models predict magnetic fields that are inconsistent with observations. They show that the halo region likely requires its own component in a galactic field model, rather than being a simple extension of the disc field. Observations of external galaxies show that an additional out-of-plane component is also required (Beck, 2009; Krause, 2009), see e.g. Figure 1.4 (right).

A 3 component (disc + halo + out-of-plane) galactic field model has been built by Jansson & Farrar (2012). They optimised their model with combined Faraday rotation measure and polarized synchrotron emission data from WMAP7 (Komatsu et al., 2011), and their model can reproduce the observed field orientations and strengths in the Milky Way. This galactic field model suggests that field strengths in the halo region are $\lesssim 1\mu$G (see e.g. Figure 6 in Jansson & Farrar, 2012), and decrease further away in the halo. Their galactic field model also predicts polarisation maps that resemble those present in external galaxies such as NGC 891 (see e.g. Figure 1.4, right).

Faraday rotation measures have furthermore been used to infer field strengths near HVCs in the Milky Way, see Figure 1.4 (left). Betti et al. (2019) found field strengths in excess of 5 $\mu$G at the head of the Smith Cloud, and $\sim 3$ $\mu$G alongside the cloud. Betti et al. (2019) argue that the magnetic field is possibly "draped" around the head of the cloud, which amplifies the field significantly. This amplified field can become dynamically important and is expected to provide additional stability against cloud disruption. This stability against disruption and field amplification by a magnetic draping effect is also seen in numerical studies of moving cold clouds in a hot medium (e.g. Dursi & Pfrommer, 2008; Banda-Barragán, 2016; Grønnow et al., 2017; Grønnow et al., 2018).

Both the observational findings and the numerical predictions indicate that magnetic fields can have an important effect on the evolution of CGM clouds and should not be ignored.

## 1.2  The Cloud-Wind Problem

Numerical studies are well-suited to further our understanding of the interactions between the cold gas clouds and the hot halo. The general approach is with "cloud-wind" simulations, where a cold ($T \sim 10^4$ K) cloud is initialised at rest with respect to a moving hot, surrounding medium (see Figure 1.5 for a schematic view). Note that this setup is equivalent to a moving cloud in a static medium. The primary effects on the evolution of these systems are expected to be radiative cooling, thermal conduction, magnetic fields, and in some cases self-gravity (Li et al., 2019).
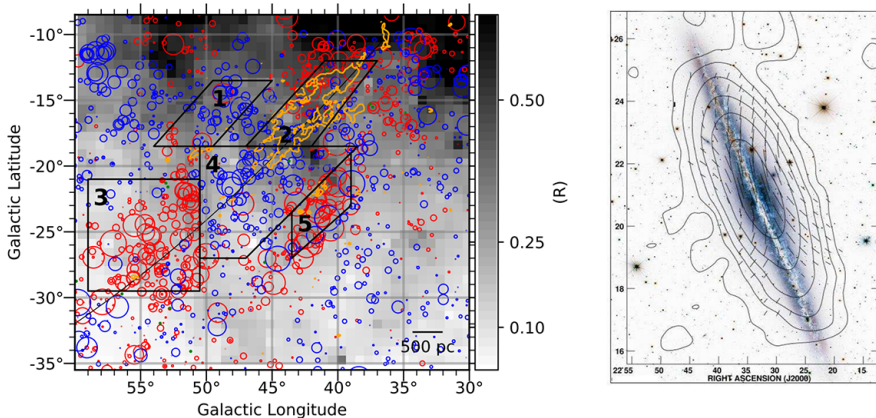
*Figure 1.4: On the left we show Wisconsin Hα Mapper Northern Sky Survey (WHAM-NSS, Haffner et al., 2003) Hα emission measures (grey scale), that are overlaid with a Green Bank Telescope H I emission contour at $v_{\text{GSR}} = +247$ in orange, and Faraday rotation measures in red (positive) and blue (negative). The black polygons denote distinct regions of interest. The opposite signs of the rotation measures in polygons 1 and 5, positioned alongside the head of the cloud (polygon 2) are thought to be evidence of a magnetic draping effect (Figure from Betti et al., 2019). On the right, we show radio continuum emission contours of NGC 891 obtained using the 100-meter Effelsberg telescope (Figure adapted from Krause, 2009, copyright: MPIfR, Bonn), overlaid on an optical image of NGC 891 taken by the Canada-France-Hawaii Telescope (Credit: CFHT/Coelum, 1999). The magnetic field orientation is overlaid showing a roughly "X" shape, which indicates that an out-of-plane component for galactic magnetic field models is necessary.*

In the literature, two distinct cases of "cloud-wind" simulations are sometimes wrongfully assumed to be the same. This concerns "cloud-shock" and "cloud-wind" simulations. The difference is that in the cloud-shock case, there is an initial shock that interacts with the cloud, and after this a wind. This shock is not present in the cloud-wind simulations. These two setups were generally believed to be comparable, however a recent investigation by Goldsmith & Pittard (2017) shows that the shock does in fact change the evolution of the system. Throughout this thesis we refer typically to works that perform cloud-wind simulations unless specifically stated otherwise.

### 1.2.1 Radiative processes

The inclusion of radiative cooling in cloud-wind simulations has been found to stabilise the cloud by damping sound waves (Vietri et al., 1997), and enhancing pressure support leading to longer cloud lifetimes (Cooper et al., 2009). While moving through the hot halo, gas is stripped from the cloud by Kelvin-Helmholtz instabilities, which can then mix efficiently with the hot halo gas and trigger its condensation. This increases the total amount of cold gas in the simulation domain (e.g. Marinacci et al., 2010), which means that these clouds can play an important role in the galactic fountain cycle (see Figure 1.3).

Radiative cooling has furthermore been found to fragment cold gas through thermal instability (Field, 1965) to a characteristic scale $l \sim 0.1\text{pc}/n$ (McCourt et al., 2018), where $n$ is the number density of cold material. This shattering process potentially explains the observed column densities and the large covering fractions of Lyman-$\alpha$ absorption in galactic halos (see e.g. McCourt et al., 2018; Sparre et al., 2018).
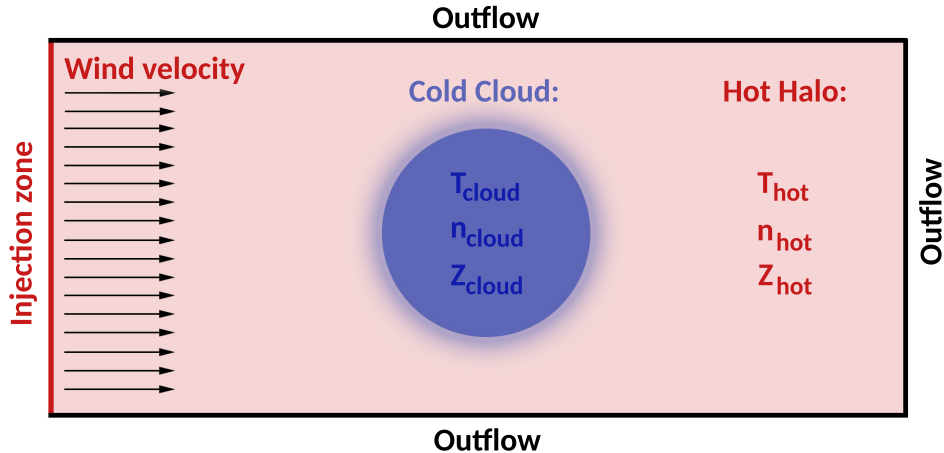
*Figure 1.5: A schematic view of the cloud-wind problem in 2D. The cloud is initialised in pressure equilibrium with the surrounding hot halo. The hot halo is initialised with a velocity relative to the stationary cold cloud. At the injection zone (red line) we update the domain with the physical conditions of the hot halo. All other boundaries are configured as outflow boundaries.*

### 1.2.2 Thermal conduction

Thermal conduction is a diffusive heat exchange process that takes place in the presence of strong temperature gradients. It is therefore expected to play a fundamental role in the evolution of the CGM due to the large temperature difference between the cold cloud and the hot halo, and has been included by several authors (e.g. Vieser & Hensler, 2007; Brüggen & Scannapieco, 2016; Armillotta et al., 2016; Armillotta et al., 2017; Li et al., 2019; Liang & Remming, 2020). Notably, thermal conduction introduces a new characteristic scale, the Field length (Field, 1965; Begelman & McKee, 1990). If a cloud has a size that is larger than the Field length, radiative cooling will be dominant. However, if the size of the cloud is smaller than the Field length then thermal conduction will be dominant, which likely causes the cloud to evaporate. Since the Field length is typically of the order of $\sim 20$ pc in the CGM (generally much larger than the 0.1 pc/$n$ as predicted by McCourt et al., 2018), this might significantly suppress the shattering process as described in Section 1.2.1.

Additionally, it has been found that thermal conduction can form an evaporative layer between the hot halo and the cold cloud, which smoothes out the temperature- and thus the density-gradient, thereby suppressing the formation of KH instabilities (Vieser & Hensler, 2007). This hinders the destruction of the clouds and can extend their lifetime (Armillotta et al., 2017, see e.g. Figure 1.6).

### 1.2.3 Magnetic fields

Early 2D simulations involving adiabatic magneto-hydrodynamical (MHD) flow (Mac Low et al., 1994; Jones et al., 1996) found that magnetic fields can also suppress the formation of KH instabilities leading to longer cloud lifetimes. The magnetic field was found to form flux ropes around the cloud in a process called magnetic draping (Dursi & Pfrommer, 2008), and is strongly amplified at the cloud-halo interface. This region of amplified field strength effectively shields the cloud from collapse due to the strong magnetic pressure.

It has been found by McCourt et al. (2015) that tangled magnetic fields delay the disrup-

tion of the clouds. This was investigated further by Banda-Barragán et al. (2017), who have shown that stronger tangled magnetic fields in the cloud increase the magnetic shielding effect and thus lead to longer lifetimes. More recently, Grønnow et al. (2018) studied the effect of magnetic fields on galactic fountain clouds and found that magnetic fields can reduce the amount of cold gas that is produced by condensation. The effect of magnetic fields is thus important when simulating cold clouds moving in the CGM.

## 1.3 Goal of this thesis

The inclusion of radiative cooling, magnetic fields and thermal conduction in simulations is complicated and has only recently been investigated in 2D (Liang & Remming, 2020), and in 3D (Li et al., 2019). The complication arises from the nature of thermal conduction in the presence of magnetic fields. Thermal conduction is dominated by the contributions of free electrons, that preferentially move along magnetic field lines (Spitzer, 1962). The heat flux in the presence of magnetic fields is thus highly anisotropic, being strongly suppressed perpendicularly to field lines (see Section 2.4 for a detailed description). A simple approximation is often made to account for this in hydrodynamical (HD) simulations with isotropic thermal conduction in the form of an efficiency factor $f$. Galactic magnetic fields are expected to be "tangled" due to turbulent gas flows leading to locally amplified, disordered fields (e.g. Klessen & Hennebelle, 2010). Anisotropic thermal conduction in a tangled magnetic field can thus be approximated as isotropic, but at a lower efficiency $f$. Based on this assump-



*Figure 1.6: Simulation including thermal conduction by Armillotta et al. (2017) that shows the temperature evolution over time of a 2D cloud travelling through the CGM of a typical Milky-Way like galaxy.*

tion, it was shown by Narayan & Medvedev (2001) that the efficiency of thermal conduction can be reduced to $20\%$ ($f \approx 0.20$) of the classical Spitzer value if the turbulence occurs at many scales. Other authors find that thermal conduction is much less efficient at $0.1 - 1\%$ ($f \approx 0.001 - 0.01$) of the Spitzer value (Chandran & Cowley, 1998).

The interaction between the hot halo and a moving cloud can stretch and significantly amplify magnetic field lines (see e.g. Asai et al., 2007), such that the field experienced by the cloud is no longer tangled. Therefore the overall efficiency of thermal conduction in these systems is hard to pin-point. Previous works that use this approximation utilised an intermediate value of $10\%$ (e.g. Armillotta et al., 2016; Armillotta et al., 2017).

In this work we investigate the merit of the approximation of a global $f$-factor by running a large suite of fully 3D HD and MHD simulations of cloud-wind systems representative of the conditions in the CGM. Our main goal is to compare the evolution between HD and MHD simulations, focussing specifically on the evolution of the cold gas mass.

Since we include radiative cooling in all of our simulations, the net amount of cold gas will generally increase (condensation, e.g. Marinacci et al., 2010), as opposed to decrease (evaporation). However, given that both thermal conduction (Armillotta et al., 2016), and magnetic fields (Grønnow et al., 2018) have been shown to suppress condensation, the quantification of this reduction is a primary goal in this thesis.

# Chapter 2

# (Magneto-)hydrodynamics

The complexity of CGM dynamics makes it natural to reach for idealised numerical simulations to help. In this section we describe the physics of (magneto-)hydrodynamics, and how the resulting equations can be solved numerically.

## 2.1 Hydrodynamical flow

Fluids are governed by the complex and non-linear Navier-Stokes equations. These equations consist of the conservation laws of mass, momentum, and energy and have to be solved simultaneously. Excluding external forces (i.e. gravity) and viscosity, the Navier-Stokes equations simplify to the Euler equations. Thus, the equations to solve for the conservation of mass, momentum and energy, respectively, for purely hydrodynamical flow are

$$\frac{\partial \rho}{\partial t} + \boldsymbol{\nabla} \cdot [\rho \boldsymbol{v}] = 0, \tag{2.1}$$

$$\frac{\partial [\rho \boldsymbol{v}]}{\partial t} + \boldsymbol{\nabla} \cdot [\rho \boldsymbol{v} \boldsymbol{v} + \boldsymbol{I} P] = 0, \tag{2.2}$$

$$\frac{\partial E}{\partial t} + \boldsymbol{\nabla} \cdot [(E + P) \boldsymbol{v}] = 0, \tag{2.3}$$

where $\rho$ is the mass density, $t$ is the time, $\boldsymbol{v}$ is the velocity vector, $P$ is the thermal pressure, $\boldsymbol{I}$ is an identity matrix, and $E$ is the energy density given by $E = \rho \varepsilon + \rho \boldsymbol{v}^2$, where $\varepsilon$ is specific internal energy. The system of equations is closed with an ideal equation of state

$$P = (\gamma - 1) \rho \varepsilon, \tag{2.4}$$

where $\gamma$ is the adiabatic index given by

$$\gamma = \frac{c_{\mathrm{p}}}{c_{\mathrm{v}}}, \tag{2.5}$$

where $c_{\mathrm{p}}$ is the heat capacity at constant pressure, and $c_{\mathrm{v}}$ is the heat capacity at constant volume.

Hydrodynamical flow in cloud-wind systems is characterised by several parameters. Firstly, the adiabatic index as described above. Secondly, the Mach-number:

$$\mathcal{M}_{\mathrm{hot}} \equiv \frac{v_{\mathrm{rel}}}{c_{\mathrm{s}}}. \tag{2.6}$$

17

where $v_{\rm rel}$ is the relative velocity between cloud and hot halo, and $c_{\rm s} \approx \sqrt{\gamma \frac{P}{\rho}}$ is the sound speed in the hot medium. Thirdly, the density contrast $\chi$ between cloud and hot halo:

$$\chi \equiv \frac{n_{\rm cloud}}{n_{\rm hot}}, \tag{2.7}$$

where $n_{\rm cloud}$ is the number density of the cloud, and $n_{\rm hot}$ is the number density of the hot halo (Jones et al., 1996).

## 2.2 Magneto-hydrodynamical flow

As described in Section 1.1.4, galactic magnetic fields are likely important in the dynamics of the CGM. As such, they should be included in the description of fluids. Throughout this thesis we assume ideal (i.e. non-resistive) magneto-hydrodynamics.

The equations for flow including magnetic fields assuming ideal MHD for conservation of mass, momentum, energy and magnetic flux, respectively become

$$\frac{\partial \rho}{\partial t} + \boldsymbol{\nabla} \cdot [\rho \boldsymbol{v}] = 0, \tag{2.8}$$

$$\frac{\partial [\rho \boldsymbol{v}]}{\partial t} + \boldsymbol{\nabla} \cdot [\rho \boldsymbol{v} \boldsymbol{v} - \boldsymbol{B} \boldsymbol{B} + \boldsymbol{I} P] = 0, \tag{2.9}$$

$$\frac{\partial E}{\partial t} + \boldsymbol{\nabla} \cdot [(E + P)\boldsymbol{v} - \boldsymbol{B}(\boldsymbol{v} \cdot \boldsymbol{B})] = 0. \tag{2.10}$$

$$\frac{\partial \boldsymbol{B}}{\partial \mathsf{t}} = \boldsymbol{\nabla} \times (\boldsymbol{v} \times \boldsymbol{B}), \tag{2.11}$$

where in this case $P = P_{\rm th} + P_{\rm mag}$, and $P_{\rm mag} = \frac{1}{2}|\boldsymbol{B}^2|$[1] is the magnetic pressure, and $E = \rho \varepsilon + \rho v^2 + \frac{1}{2}|\boldsymbol{B}|^2$. The MHD equations are closed with the same ideal equation of state as described by Eqn. 2.4.

Note that the terms $-\boldsymbol{\nabla} \cdot (\boldsymbol{B}\boldsymbol{B}) + \boldsymbol{\nabla} \cdot \left(\frac{1}{2}|\boldsymbol{B}|^2\right)$ in the (Cauchy) momentum equation (Eqn. 2.9), where I have substituted $P_{\rm mag} = \frac{1}{2}|\boldsymbol{B}|^2$, may be rewritten more intuitively as

$$(\boldsymbol{\nabla} \times \boldsymbol{B}) \times \boldsymbol{B} = -\boldsymbol{\nabla} \cdot \left(\frac{1}{2}|\boldsymbol{B}|^2\right) + (\boldsymbol{B} \cdot \boldsymbol{\nabla})\boldsymbol{B}, \tag{2.12}$$

where we have used the vector identities

$$\boldsymbol{\nabla}(\boldsymbol{a} \cdot \boldsymbol{b}) = (\boldsymbol{a} \cdot \boldsymbol{\nabla})\boldsymbol{b} + (\boldsymbol{b} \cdot \boldsymbol{\nabla})\boldsymbol{a} + \boldsymbol{a} \times (\boldsymbol{\nabla} \times \boldsymbol{b}) + \boldsymbol{b} \times (\boldsymbol{\nabla} \times \boldsymbol{a}), \tag{2.13}$$

$$\boldsymbol{a} \times \boldsymbol{b} = -\boldsymbol{b} \times \boldsymbol{a}, \tag{2.14}$$

and

$$(\boldsymbol{a} \times \boldsymbol{b}) \times \boldsymbol{c} = \boldsymbol{b}(\boldsymbol{c} \cdot \boldsymbol{a}) - \boldsymbol{a}(\boldsymbol{c} \cdot \boldsymbol{b}). \tag{2.15}$$

The term $(\boldsymbol{\nabla} \times \boldsymbol{B}) \times \boldsymbol{B}$ in Eqn. 2.12 is the MHD Lorentz force, and we denote this as $\boldsymbol{f}_{\rm Lorentz}$:

$$\boldsymbol{f}_{\rm Lorentz} = (\boldsymbol{\nabla} \times \boldsymbol{B}) \times \boldsymbol{B}. \tag{2.16}$$

We may now interpret the individual terms. We notice that the first term on the right hand side in Eqn. 2.12 contains a term of which the negative gradient is a force, and corresponds

---

[1]Note that throughout this thesis we do not include the normalisation factor $1/\sqrt{4\pi}$ in equations involving $\boldsymbol{B}$.

to a magnetic pressure force. The second force term is more complicated. This term reacts to changes in the field strength along the magnetic field lines, and is referred to as a tension force. This tension force acts to straighten curved field lines.

The addition of magnetic fields results in an additional equation governing the evolution of the fluid: the magnetic induction equation. This can be interpreted as representing the conservation of magnetic flux in a comoving volume element. The magnetic field lines are said to be "frozen" in the fluid, meaning that they must move with the plasma. Note that this only holds for non-resistive MHD. The magnetic induction equation (Eqn. 2.11) becomes more intuitive when we take the gradient of it, resulting in

$$\frac{\partial}{\partial t}\left(\boldsymbol{\nabla}\cdot\boldsymbol{B}\right)=0, \tag{2.17}$$

and thus the solenoidal constraint ($\boldsymbol{\nabla}\cdot\boldsymbol{B}=0$), stating that there are no magnetic monopoles, is automatically incorporated. That is, the rate of change of the divergence of the magnetic field is kept constant, and hence as long as the initial conditions are divergence free it will stay divergence free.

In addition to the three characteristic flow parameters introduced in Section 2.1, MHD introduces one more: the plasma-$\beta$ parameter

$$\beta \equiv \frac{P_{\text{th}}}{P_{\text{mag}}}, \tag{2.18}$$

which quantifies how dynamically important a magnetic field is. A related, but important quantity is the Alfvénic Mach-number $\mathcal{M}_A$, defined as

$$\mathcal{M}_A \equiv \frac{v_{\text{rel}}}{v_A}, \tag{2.19}$$

where $v_A = \frac{|\boldsymbol{B}|}{\sqrt{\rho_{\text{hot}}}}$ is the Alfvén velocity in the hot halo. The Alfvén velocity is the characteristic velocity of Alfvén waves (Alfvén, 1942). Alfvén waves are generated by the magnetic restoring force (i.e. the tension force from the term $(\boldsymbol{B}\cdot\boldsymbol{\nabla})\boldsymbol{B}$ in Eqn. 2.12) when magnetic field lines are perturbed. The Alfén wave travels in the direction of the field lines.

Alongside Alfvén waves, two other linear waves exist in MHD: the fast and slow magnetosonic waves. These waves are the MHD equivalent of HD sound waves. The slow magnetosonic wave is *sub*-Alfvénic (i.e. $v_{\text{slow}} < v_A$), and the fast magnetosonic wave is *super*-Alfvénic (i.e. $v_{\text{fast}} > v_A$). In the limit $B \longrightarrow 0$ the Alfvén velocity is zero ($v_A = 0$), the slow magnetosonic wave ceases to exist, and the fast magnetosonic wave reduces to the normal hydrodynamical sound wave moving at the sound speed $c_{\text{s}}$.

## 2.3 Hydrodynamical instabilities

Clouds in cloud-wind simulations are stripped and ultimately destroyed by hydrodynamical instabilities. In this section the two typically most dominant instabilities are described and showcased.

### 2.3.1 Kelvin-Helmholtz instability

The Kelvin-Helmholtz (KH, Helmholtz, 1868; Kelvin, 1871) instability is very important in cloud-wind systems: the initial stripping of gas from the clouds happens by the Kelvin-Helmholtz instability. The onset of the instability is by shear flow between fluid layers that
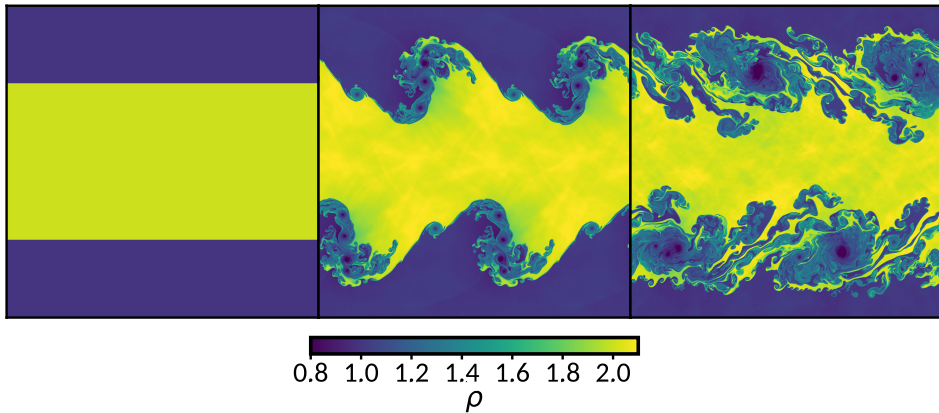
*Figure 2.1: Time snapshots of the 2D Kelvin-Helmholtz instability, performed with the PLUTO simulation code. The higher density fluid (yellow) is moving to the right, whereas the lower density fluid is moving to the left. We show the initial conditions (left), the primary billow (middle), and the turbulent mixing phase (right). Notice the secondary KH billows forming on top of the primary billows.*

typically have different densities. The instability grows exponentially until the main billow breaks (see e.g. Chandrasekhar, 1961), which leads to turbulent mixing of the two fluid layers downstream. We show time snapshots of a high-resolution run of the KH instability in Figure 2.1, as performed with the PLUTO code (Mignone et al., 2007; Mignone et al., 2011). The instability in this case was seeded by a velocity perturbation similar to what was used in Schaal et al. (2015).

### 2.3.2 Rayleigh-Taylor instability

The Rayleigh-Taylor (RT, Rayleigh, 1882; Taylor, 1950) instability is also important in the interactions between the cloud and the wind. The RT instability is triggered when the interface between two fluid layers with differing densities is subjected to an acceleration (see e.g. Chandrasekhar, 1961). This setup is only unstable if the acceleration is directed from the low density fluid towards the higher density fluid (Drazin, 2002; Drazin & Reid, 2004). In this case, the low density wind is impinging on the cloud and accelerates it, and is thus unstable. We show time snapshots of a high-resolution run of the RT instability in Figure 2.2. This was performed using the PLUTO code, where we have used the initial conditions provided by Mignone et al. (2011), based on Stone & Gardiner (2007).

## 2.4 MHD thermal conduction

In this section we describe the physics of thermal conduction for both the isotropic (HD) and the anisotropic (MHD) cases.

The thermal conduction heat flux at the temperatures we are considering is dominated by electrons (see e.g. Figure 8 in Salz et al., 2015). Since electrons are charged particles, they will experience a magnetic force when moving through a magnetic field. This magnetic force is perpendicular to the magnetic field and the velocity $\boldsymbol{v}$ of the electron ($\boldsymbol{F}_{\mathrm{Lorentz}} = e\boldsymbol{v} \times \boldsymbol{B}$, where $e$ is the charge of the electron). Therefore, electrons will either move on helical paths along magnetic field lines, or follow them directly. The constrained
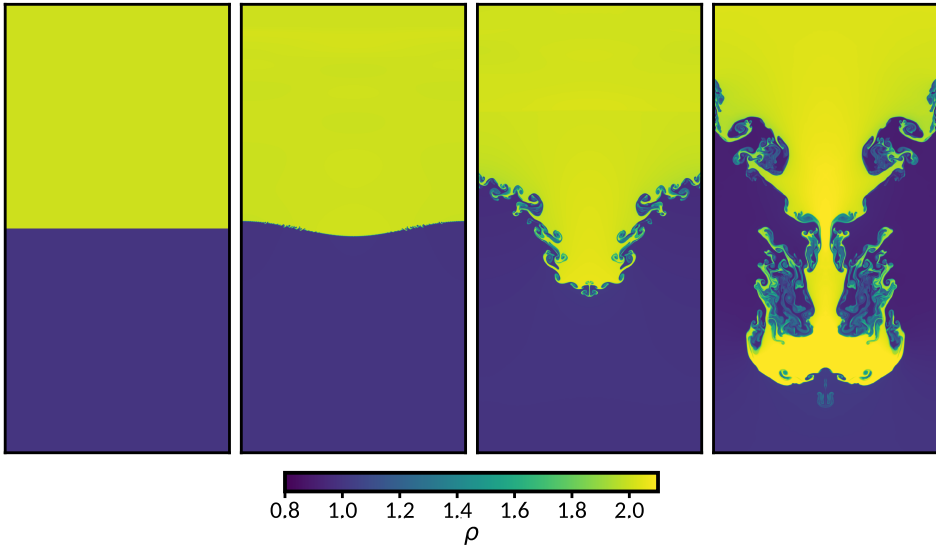
*Figure 2.2: Time snapshots of the Rayleigh-Taylor hydro-dynamical instability in 2D as performed with the PLUTO code. We show the dimensionless density ($\rho$). A gravitational potential is initialised at the bottom of the figure, such that the gravitational acceleration $\boldsymbol{g}$ is pointed downwards. The lower density fluid wants to rise, and the higher density fluid wants to fall, leading to the RT instability. Also notice the secondary Kelvin-Helmholtz instabilities that form alongside the RT instability.*

motion of electrons thus makes thermal conduction in the presence of magnetic fields highly anisotropic.

Anisotropic thermal conduction is modelled by splitting the heat flux into parallel ($\kappa_\parallel$) and perpendicular ($\kappa_\perp$) components with respect to the orientation of the magnetic field (Spitzer, 1962; Braginskii, 1965):

$$\boldsymbol{F}_{\text{class}} = \kappa_\parallel \hat{\boldsymbol{b}}(\hat{\boldsymbol{b}} \cdot \boldsymbol{\nabla} T) + \kappa_\perp [\boldsymbol{\nabla} T - \hat{\boldsymbol{b}}(\hat{\boldsymbol{b}} \cdot \boldsymbol{\nabla} T)], \tag{2.20}$$

where $\boldsymbol{F}_{\text{class}}$ is the classical conduction heat flux, $T$ is the temperature, $\hat{\boldsymbol{b}} = \boldsymbol{B}/|\boldsymbol{B}|$ is a unit vector denoting the direction of the magnetic field, and $\kappa_\perp$ and $\kappa_\parallel$ are the perpendicular and parallel components of the conductivity, respectively. Thermal conduction is at Spitzer value along the field lines $\kappa_\parallel = \kappa_{\text{Sp}}$, where

$$\kappa_{\text{Sp}} = 1.84 \times 10^{-5} \frac{T_e^{5/2}}{\ln \Psi} \quad \text{ergs/s/K/cm}, \tag{2.21}$$

where $T_e$ is the electron temperature, and $\ln \Psi$ is the Coulomb logarithm given by

$$\ln \Psi = 29.7 + \ln \left[ \frac{1}{\sqrt{n_e/\text{cm}^{-3}}} \frac{T_e}{10^6 \text{K}} \right], \tag{2.22}$$

where $n_e$ is the electron number density. Perpendicular to the field lines, the magnitude of the conductivity is much smaller

$$\kappa_\perp = \frac{8\sqrt{\pi m_H k_B} n_H^2 e^2 c^2 \ln \Psi}{3|\boldsymbol{B}^2|\sqrt{T}}, \tag{2.23}$$

where $m_H$ is the mass of hydrogen, $k_B$ is Boltzmann's constant, $n_H$ is the hydrogen number density, and $c$ is the speed of light in vacuum. For the parameters used in our analysis, $\frac{\kappa_\perp}{\kappa_\parallel} \lesssim 10^{-9}$.

When the mean free path of electrons becomes similar to or greater than the temperature scale height, the classical Spitzer flux is no longer accurate and the heat flux is said to be saturated. We account for saturated heat flux according to the description as given by Cowie & McKee (1977), and we set

$$F_{sat} = 5\phi_{sat}\rho c_s^3, \tag{2.24}$$

where $F_{sat}$ is the saturated heat flux, $\rho$ is the gas density, $c_s$ is the isothermal sound speed, and $\phi_{sat}$ is a factor of order unity that accounts for uncertainties regarding the flux-limited treatment. To ensure a smooth transition between the classical and saturated regimes, the total heat flux $\boldsymbol{F}_c$ is written as

$$\boldsymbol{F}_c = \frac{F_{sat}}{F_{sat} + |\boldsymbol{F}_{class}|}\boldsymbol{F}_{class}. \tag{2.25}$$

For HD simulations (without magnetic fields), thermal conduction is often assumed to be isotropic. The argument is that small scale turbulence in a magnetic field can make the total heat flux roughly isotropic. This isotropic thermal conduction must be suppressed with respect to the classical Spitzer heat flux, since thermal conduction is only at Spitzer value along field lines. Therefore, a typical assumption is made that quantifies this suppression in the form of an efficiency factor $f$. This is included in the equation for the isotropic thermal conduction heat flux as

$$\boldsymbol{F}_c = f\frac{F_{sat}}{F_{sat} + |\boldsymbol{F}_{class}|}\boldsymbol{F}_{class}, \tag{2.26}$$

where in the isotropic thermal conduction case Eqn. 2.20 reduces to $\boldsymbol{F}_{class} = \kappa_{Sp}\boldsymbol{\nabla}T$.

## 2.5 Numerical implementation

Analytical solutions to the equations governing fluids described above can only be derived in specific cases (e.g. the 1D Sod shock tube, Sod, 1978). However, these partial differential equations can be solved numerically. The most common ways the equations are solved is using grid-based methods implemented in codes such as ATHENA (Stone et al., 2008), or PLUTO (Mignone et al., 2007; Mignone et al., 2011), via smoothed-particle hydrodynamics codes (e.g. GASOLINE, Wadsley et al., 2017), or via moving mesh hydrodynamics codes (e.g. AREPO, Weinberger et al., 2020). In this thesis we will focus on grid-based codes, typically called Godunov-type (Godunov, 1959). The main requirements for a grid-based fluid code are a Riemann solver, flux limiter, reconstruction scheme, and time integrator.

### 2.5.1 Riemann solvers

A Riemann problem consists of an initial value problem where there exists a conservation law over a certain discontinuity. Riemann problems arise naturally in finite-volume schemes, where cells containing physical quantities are discrete and cell-boundaries are discontinuities. Riemann problems are solved by Riemann solvers. Solutions to Riemann problems can be exact (e.g. Godunov, 1959), but they are more typically solved approximately using a variety of methods, such as Roe (1981), or the Harten, Lax, van Leer (HLL)
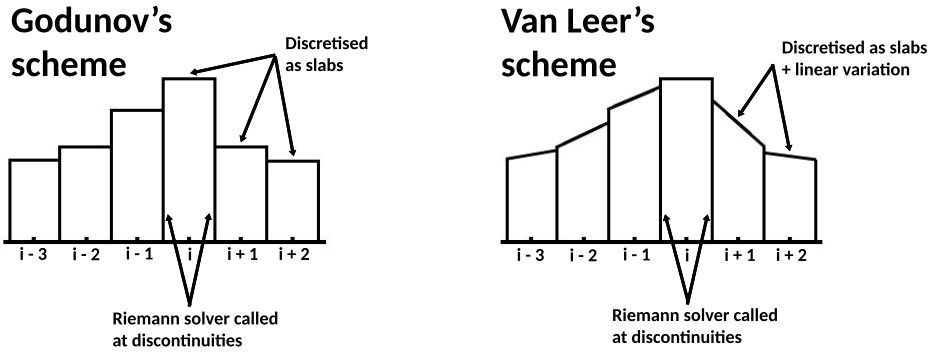
Figure 2.3: *A comparison between 1st order Godunov's scheme (left), and van Leer's 2nd order scheme (right). Godunov's scheme assumes flow variables to be cell-centered, whereas van Leer's scheme assumes a linear variation of the flow variables over the cell.*

based approximate solvers (Harten et al., 1983; Einfeldt, 1988; Toro et al., 1994; Miyoshi & Kusano, 2005, HLL, HLLE, HLLC, HLLD, respectively). The solutions to the Riemann problem consist of a set of characteristic waves (e.g. Lax, 1957). These consist of shock waves, rarefaction waves and contact waves. The HLL based solvers listed above approximate the solutions to the Riemann problems by only considering some of these waves. The HLLC solver for example restores the contact wave which is not included in the HLL solver. Furthermore, the HLLD solver is extended to work for MHD, and corresponds to the HLLC solver when the magnetic field vanishes.

## 2.5.2 Reconstruction and slope limiting

The left and right states of the Riemann problem in Godunov's scheme were originally determined by simply taking the cell-centered quantities (see Figure 2.3, Godunov, 1954, 1959). Attempts at creating higher order schemes were met with under-and over-shooting near discontinuities (i.e. they are not "monotone", e.g. Lax & Wendroff, 1960). Godunov proved in a theorem now called Godunov's theorem that a linear, monotone scheme is accurate to at most first order (Godunov, 1954, 1959). First order methods are generally considered inaccurate for fluid codes, and are called numerically diffusive. Numerical diffusion closely resembles physical diffusion because a limited resolution causes flow variables to be smoothed out. Because Godunov's scheme is only first order accurate, and due to the slow iterative nature of finding solutions it was not used much, until a 2nd order Godunov type scheme was developed by van Leer (1977, 1979). This scheme gives the originally cell-centered variables a linear profile over every zone, such that it is now second order accurate in space, see Figure 2.3. Monotonicity is maintained by limiting the slope using a slope limiter and keeping a small jump between cells. Van Leer's scheme is part of the Monotone Upstream-Centered Schemes (MUSCL) and is still used today (e.g. Krause, 2019, and this work). Other schemes that are commonly used are e.g. Weighted Essentially Non-Oscillatory schemes (WENO, e.g. Shu, 1998; Jiang & Wu, 1999; Shu, 2009).

## 2.5.3 Time integration

Time integration for any system of partial differential equations can be performed *explicitly* or *implicitly*. In *explicit* schemes time is evolved explicitly, e.g. $t_{\text{new}} = t + \Delta t$. The new

state of the system is thus calculated from the old state. This method is straight forward to implement, but can be more restrictive in terms of the allowed maximum timestep. The timestep is restricted to a stability constraint: The Courant, Friedrichs, Lewy condition (CFL, Courant et al., 1928). This stability constraint can be generalised to $N$ dimensions and reads

$$\text{CFL} = \Delta t \left( \sum_{i=1}^{N} \frac{\lambda_{l_i}}{\Delta l_i} \right) \leq \text{C}_{\text{max}}, \tag{2.27}$$

where $\lambda_{l_i}$ is the largest wave speed (a "wave" being one of the solutions to the Riemann problem, as described in Section 2.5.1), and $\Delta l_i$ is the physical size of the cell. The interpretation is relatively straightforward: in a time $\Delta t$, the wave with the largest speed cannot cross a distance larger than the cell length. The value of $\text{C}_{\text{max}}$ is typically below unity, and depends largely on the dimensionality, and the scheme used.

It is clear that for flows with large flow velocity or fast shocks, the timestep must decrease. Similarly, for high-resolution simulations where $\Delta l_i$ is small, the time step will also decrease. Therefore, in fluid simulations an increase in resolution has a two-fold effect. The number of cells increases, and the maximum timestep decreases, which both directly affects how many calculations have to be performed. Additional physics can furthermore affect the maximum timestep, which we discuss further in Section 3.2.

In *implicit* schemes an additional equation must be solved including both the initial and the later state:

$$f\big(x(t), x(t + \Delta t)\big) = 0, \tag{2.28}$$

where one solves for the later state $x(t + \Delta t)$ using a root-solver (e.g. Brent's method Brent, 1971). The implicit integration scheme introduces additional computational steps, but has fewer timestep restrictions than the explicit scheme. The implicit scheme can also be hard to implement, and does not work for every operator. In this work we have used the explicit scheme.

# Chapter 3

# Methods

## 3.1 Simulation Code

We use PLUTO version 4.3 (Mignone et al., 2007; Mignone et al., 2011) to solve the system of equations for hydro-dynamical (HD) and magneto-hydrodynamical (MHD) flow in 3 spatial dimensions. PLUTO is a grid-based Godunov-type (Godunov, 1959) code, i.e. a conservative finite-volume method that solves exact or approximate Riemann problems at each inter-cell boundary. For both HD and MHD flows we close the system of equations with an ideal equation of state. For the internal energy we assume that both the cloud and hot halo are monatomic and accordingly set the adiabatic index $\gamma = 5/3$. In MHD runs we approximately enforce the solenoidal constraint ($\nabla \cdot \mathbf{B} = 0$) using the hyperbolic divergence cleaning scheme by Dedner et al. (2002), implemented in PLUTO by Mignone et al. (2010). For the flux computations there is a trade-off to be made between accuracy and numerical stability, as more accurate Riemann solvers are generally also less stable. As a compromise, we employ the approximate Riemann solver HLLC for HD simulations and HLLD for MHD simulations (see Section 2.5.1). We use second-order Runge-Kutta time integration and linear (2nd order) reconstruction for all simulations (see Sections 2.5.2 and 2.5.3).

In order to run our simulations at sufficient spatial resolutions while keeping computational costs relatively low, we employ adaptive mesh refinement (AMR). We use the gradient of the density as refinement variable, and to ensure numerical stability we set the CFL number to $C_\alpha = 0.3$ for all simulations. We start our simulations from a base grid of $60 \times 20 \times 20$ on a physical grid of $6 \times 2 \times 2$ kpc, and for each level of refinement we increase the resolution in every dimension by a factor 2. In the fiducial setup we refine 5 times to an equivalent resolution of $1920 \times 640 \times 640$. In this way, there are 32 cells per cloud radius ($\mathcal{R}_{32}$), which gives a spatial resolution of $\sim 3$ pc/cell at the highest refinement level. We show an example of mesh refinement for a typical simulation in Figure 3.1.

## 3.2 Numerical simulations

We initialise our simulations according to the typical "cloud-wind" problem, see e.g. Figure 1.5, and follow the general setup as described in Grønnow et al. (2018). Since the simulation setup is very similar to theirs, we only go over this shortly. To prevent possible numerical instabilities produced by sharp gradients between halo and cloud, we initialise a smooth transition in the density profile. We use a similar transition as in Grønnow et al.
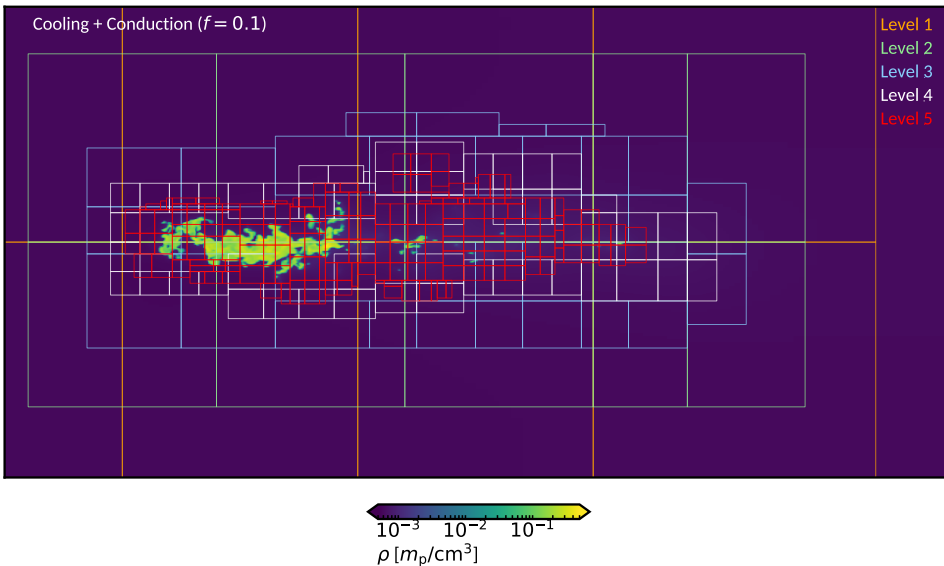
Figure 3.1: *A slice through the density for a typical simulation. We highlight the different levels of refinement by color, and show the encompassing 'boxes' that can each contain at most $32^3$ cells. Note how the region that harbours the cold gas (cloud + wake) are resolved at the highest level.*

(2018), and set

$$\rho(r) = \rho_{\mathrm{hot}} + \frac{1}{2}(\rho_{\mathrm{cloud}} - \rho_{\mathrm{hot}}) \times \left(1 - \tanh\left[s\left(\frac{r}{r_0} - 1\right)\right]\right), \tag{3.1}$$

where $r$ is the radius from the center of the cloud, $r_0 = 100$ pc is the cloud radius used in the simulations, tanh is the hyperbolic tangent, and $s = 10$ sets the steepness of the profile. We show the profile in Figure 3.2, along with the cloud radius and the "wind radius" ($r_{\mathrm{w}}$). The wind radius denotes the radius beyond which the hot halo is given a relative velocity (130 pc). This distinction is important because cloud material in this transition regime should not be initialised with a high velocity. If they were, metal-rich gas could mix quickly with the halo material and produce a bias in the amount of cold gas that is formed. We choose $r_{\mathrm{w}} = 130$ pc because the mass enclosed within 130 pc is $M(r < 130$ pc$) = 0.9999 \times M_{\mathrm{cloud}}$, which is sufficiently close to the cloud mass. The metallicity is assigned as a step function, where $Z(r < r_0) = Z_{\mathrm{cloud}}$ and $Z(r > r_0) = Z_{\mathrm{hot}}$, where $Z_{\mathrm{cloud}}$ and $Z_{\mathrm{hot}}$ are the metallicity of the cloud and hot gas, respectively.

Turbulent velocities with Mach-number $\mathcal{M} \approx 1$ are added to the cloud to make the simulations more realistic, and to reduce numerical artifacts that can sometimes arise from symmetry. Similar to Armillotta et al. (2016), we pick random values from a Gaussian distribution of velocities with a dispersion of 10 km/s, and a mean of 0 km/s. These velocities are assigned in the same region as the cloud metallicity ($r < r_0$). The effect of adding random motions to the cloud is evaluated in Section 4.2.

We assume cloud and halo ("wind") parameters typical of IVCs (e.g. Wakker, 2001), and that are consistent with earlier work (see e.g. Marinacci et al., 2010; Armillotta et al., 2016; Grønnow et al., 2018), as listed in Table 3.1.

We include radiative cooling in every simulation using the tabulated cooling module, based on the collisional ionization equilibrium cooling tables of Sutherland & Dopita (1993),
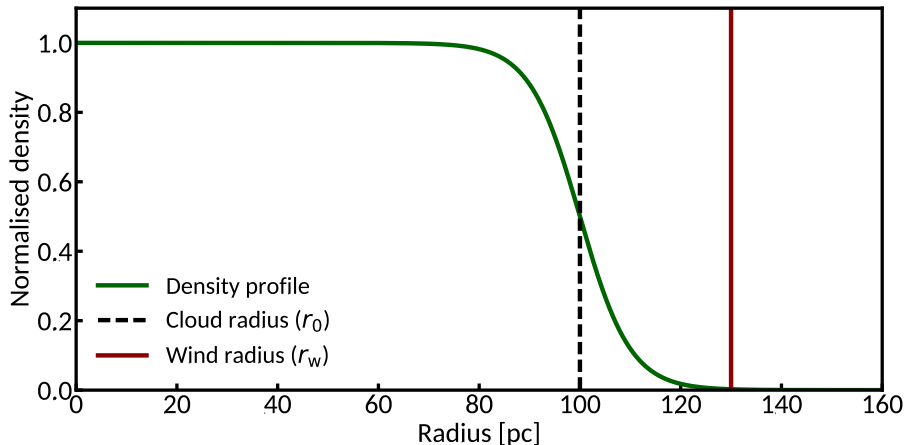
*Figure 3.2: The 1D density profile as a function of radius. The cloud radius is denoted with the black dotted line and is 100 pc in all of our simulations. At the cloud radius, $\rho \approx 0.5\rho_{\mathrm{cloud}}$. The "wind radius" is the radius beyond which we give a velocity to the halo medium. The mass contained within the wind radius is $M(r < 130\,pc) = 0.9999 \times M_{\mathrm{cloud}}$.*

*Table 3.1: The cloud and hot halo parameters for our fiducial setup. The parameters are the relative velocity between cloud and halo ($v_{rel}$), cloud temperature ($T_{cloud}$), halo temperature ($T_{hot}$), cloud/halo metallicity ($Z_{cloud/hot}$), halo number density ($n_{hot}$), and cloud radius ($r_0$). Note that the pressure equilibrium between cloud and halo makes the cloud number density a fixed value.*

| $v_{\mathrm{rel}}$ [km/s] | $T_{\mathrm{cloud}}$ [K] | $T_{\mathrm{hot}}$ [K] | $Z_{\mathrm{cloud}}$ [$Z_\odot$] | $Z_{\mathrm{hot}}$ [$Z_\odot$] | $n_{\mathrm{hot}}$ [cm$^{-3}$] | $r_0$ [pc] |
|---|---|---|---|---|---|---|
| 75 | $10^4$ | $2\times10^6$ | 1 | 0.1 | $10^{-3}$ | 100 |

displayed in Figure 3.3, on the left. The variation in mean molecular weight $\mu$ with temperature $T$ is accounted for, and we interpolate for the variation in metallicity ($Z$) with $T$ between 3 tables with metallicities $0.1Z_\odot$, $0.3Z_\odot$, $Z_\odot$, similarly to Marinacci (2011); Grønnow (2018). We keep track of the metallicity using a passive scalar $C$ that does not affect the flow, which we advect conservatively as

$$\frac{\partial(\rho C)}{\partial t} + \boldsymbol{\nabla} \cdot (\rho C \boldsymbol{v}) = 0. \tag{3.2}$$

As mentioned, we initialise the passive scalar $C$ in simulations with a cloud metallicity ($Z_{\mathrm{cloud}}$) for $r < r_0$, and $Z_{\mathrm{hot}}$ elsewhere. We finally assume a cooling floor at $T = 10^4$ K below which no cooling occurs. This assumption is justified as the cooling rate drops drastically around $10^4$ K as can be seen in Figure 3.3 on the left. It furthermore crudely corresponds to an equilibrium temperature between radiative cooling ($\propto n^2\Lambda$) and radiative heating ($\propto n\Gamma$) from the UV-background (e.g. Richings et al., 2014). Thermal conduction is included in our simulations using the readily available thermal conduction module in PLUTO, of which the source code is edited as follows. We assume that thermal conduction happens exclusively through free electrons, and we account for this by multiplying the thermal conduction heat flux (Eqn. 2.26) by the ionisation fraction $x_{\mathrm{i}}$. The ionisation fraction depends on the temperature, which we calculate using the same procedure as described for radiative cooling.

The full equation becomes

$$\boldsymbol{F}_\text{c} = f \frac{F_\text{sat} x_\text{i}}{F_\text{sat} + |\boldsymbol{F}_\text{class}|} \boldsymbol{F}_\text{class}, \tag{3.3}$$

where $f = 1$ for MHD simulations. For MHD simulations we set $\kappa_\perp = 0$. This assumption is implemented standardly by PLUTO, and is justified since $\frac{\kappa_\perp}{\kappa_\parallel} \lesssim 10^{-9}$ for the range of conditions in our simulations.

Radiative cooling and thermal conduction are included as source terms in the energy equation (Eqn. 2.10)

$$\frac{\partial E}{\partial t} + \boldsymbol{\nabla} \cdot [(E+P)\boldsymbol{v} - \boldsymbol{B}(\boldsymbol{v} \cdot \boldsymbol{B})] = \rho^2 \Lambda_\text{net} + \boldsymbol{\nabla} \cdot \boldsymbol{F}_\text{c}, \tag{3.4}$$

where $\rho^2 \Lambda_\text{net}$ is the contribution from radiative cooling, $\Lambda_\text{net}$ is the net cooling rate, and $\boldsymbol{\nabla} \cdot \boldsymbol{F}_\text{c}$ is the contribution from thermal conduction. Both introduce new constraints on the maximum timestep. Radiative cooling becomes problematic if the cooling time ($\tau_\text{cool}$, see e.g. Figure 3.3, right), given by

$$\tau_\text{cool} = \frac{\frac{3}{2} n k_\text{B} T}{n_e n_t \Lambda_\text{net}}, \tag{3.5}$$

where $n_e$ is the electron number density and $n_i$ is the ion number density, becomes smaller than the hydrodynamical timestep, since this can give rise to negative pressures or densities. Thermal conduction can impose severe restrictions on the maximum timestep when an explicit solver is used as it is a diffusive process. This restricts the maximum time step as

$$\Delta t \approx \frac{\Delta l^2}{\eta}, \tag{3.6}$$

where $\Delta l$ is the physical cell size, and $\eta$ is the diffusion coefficient. It is clear that for high resolution (i.e. $\Delta l$ is small), and strong diffusion ($\eta$ is large) the maximum timestep can become impractically small. Since PLUTO in AMR mode only has an explicit solver for thermal conduction, we have deliberately chosen relatively diffuse time integration (2nd order Runge-Kutta), and linear (2nd order) reconstruction (see Sections 2.5.2 and 2.5.3).

We vary between weak (0.1 $\mu$G) and strong (1.0 $\mu$G) magnetic fields, as appropriate for the lower part of the CGM (Grønnow et al., 2018). For each field strength we run the simulations for orientations of the magnetic field parallel ($B_\parallel$) or perpendicular ($B_\perp$) to the relative velocity. We also run one simulation with a magnetic field at $45\deg$ ($B_\text{ob}$). In simulations where we include both thermal conduction and a magnetic field, we calculate the *anisotropic* thermal conduction heat flux.

To assess the effect of isotropic thermal conduction, we perform HD simulations with either only radiative cooling, or radiative cooling and isotropic thermal conduction at several efficiencies by varying $f$, as listed in Table 3.2. To examine the effect of anisotropic thermal conduction in the presence of magnetic fields, we run MHD simulations at the field strengths and orientations as mentioned above. In this case, we set anisotropic thermal conduction either off, or at full Spitzer efficiency. Our main goal is to compare the evolution between isotropic thermal conduction runs (no magnetic field) and anisotropic thermal conduction runs (with magnetic fields).

Additionally, we explore several different cloud and halo parameters. We investigate a lower cloud metallicity, a higher relative velocity, and lower cloud- and halo-densities. For every different set of parameters, we perform the same suite of HD and MHD simulations as described above (Table 3.2).

*Table 3.2: The varied simulation parameters. The 'Setup' column describes for which module(s) we perform the variation.*

| Parameter | Setup | Values considered |
|---|---|---|
| $f$ | HD | 0.01, 0.05, 0.1, 0.15, 0.2 |
| $v_{rel}$ [1] [km/s] | HD,MHD | 75, 150 |
| $Z_{cloud}$ [$Z_\odot$] | HD,MHD | 0.1, 1.0 |
| $n_{cloud}$, $n_{hot}$ [2] [cm$^{-3}$] | HD,MHD | (0.2,10$^{-3}$), (0.1,5$\times$10$^{-4}$) |
| $|\mathbf{B_0}|$ [3] [$\mu$G] | MHD | 0.1, 1.0 |
| $B_{orientation}$ | MHD | $B_\perp$, $B_\parallel$, $B_{ob}$ |

[1] This corresponds to Mach numbers $\mathcal{M} \approx 0.35$ and 0.70 for relative velocities 75 and 150 km/s, respectively.

[2] We assume pressure equilibrium between the cloud and the hot halo, thus the density contrast between cloud and halo is in both cases $\chi = \frac{n_{cloud}}{n_{hot}} = 200$.

[3] The plasma-$\beta$ parameter, defined as the ratio between the thermal pressure of the gas over the magnetic pressure, is for the higher densities $\beta$=7 and 700 for field strengths 1 and 0.1 $\mu$G, respectively. For the lower density setup, the plasma-$\beta$ values are a factor 2 smaller.
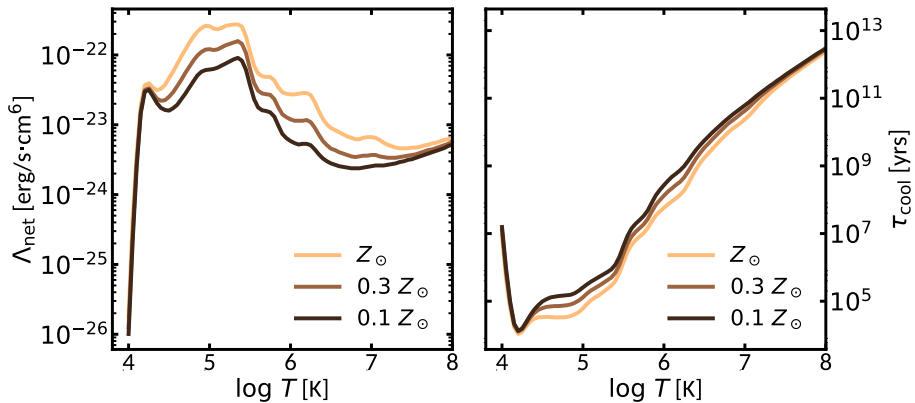


*Figure 3.3: The cooling rates for 3 different metallicities from the collisional ionisation equilibrium tables of Sutherland & Dopita (1993) (left). On the right, we show the corresponding cooling times, where the density is varied isobarically with the hot halo ($T = 2 \times 10^6$ K, and $n = 10^{-3}$ cm$^{-3}$).*

## 3.3 Diagnostics

We analyze the outputs of our simulations using volume averaged, mass weighted quantities as described in Klein et al. (1994). We focus on the evolution of the amount of cold gas in the simulation domain according to

$$\Delta M_{\text{cold}} = \frac{\int \rho_{\text{cold}} dV}{M_{\text{cloud, t=0}}}, \tag{3.7}$$

where, similarly to Armillotta et al. (2016), we denote gas as "cold" if $T < 2 \times 10^4$ K, and we normalise by the initial cloud mass $M_{\text{cloud, t=0}}$.

We furthermore calculate the mass of mixed gas similarly to Xu & Stone (1995). We define another passive scalar $C$ (Eqn. 3.2) over the simulation volume, where we set $C = 1$ inside the cloud ($r < r_0$), $C = 0$ elsewhere, and define gas to be 'mixed' if $0.1 < C < 0.9$.

To follow the evolution of simulations with different parameter setups equally, we denote time in units of cloud-crushing time $t_{\text{cc}}$ (Jones et al., 1996),

$$t_{\text{cc}} \equiv \sqrt{\chi} \frac{2r_0}{v_{\text{rel}}}, \tag{3.8}$$

where $\chi = \frac{n_{\text{cloud}}}{n_{\text{hot}}}$ is the density contrast, and $v_{\text{rel}}$ is the relative velocity between the cloud and the halo. For our fiducial setup, $t_{\text{cc}} \approx 36$ Myr. The cloud-crushing time was first defined by Klein et al. (1994), but without the factor 2 as in the numerator of Eqn. 3.8, and denotes the time for the internal shock created by the initial collision with the wind to travel across the cloud. This was used in early cloud-shock and cloud-wind simulations, since the clouds in adiabatic simulations were roughly destroyed on this timescale. However, as discussed in Section 1.2, radiative cooling, thermal conduction and magnetic fields can all have effects on the survival time of clouds. It is therefore not an accurate timescale for the destruction of clouds, but it is still useful when comparing simulations with different cloud densities and velocities.

# Chapter 4

# Technical Results

In this chapter we go over some technical tests that we have carried out with the PLUTO code. In particular, we compare the evolution between 2D and 3D simulations in Section 4.1, and we analyse the addition of turbulence in Section 4.2.

## 4.1  2D vs. 3D simulations

Some studies in the literature assume a 2D geometry as a basis for their simulations (e.g. Jones et al., 1996; Armillotta et al., 2016; Armillotta et al., 2017; McCourt et al., 2018; Liang & Remming, 2020). The main consideration is that 3D simulations are much more computationally expensive. A 2D simulation can therefore in practice be run at much higher resolution as compared to 3D simulations. In this section we investigate whether 2D simulations can provide reliable estimates in terms of their cold gas mass evolution (Eqn. 3.7) as compared to fully 3D simulations.

While the difference between 2D and 3D simulations has been investigated previously by e.g. Banda-Barragán (2016); Armillotta et al. (2016); Grønnow (2018); Sparre et al. (2018), it remains important to evaluate for different codes and simulation setups. For consistency, both the 3D and the 2D simulations are run with the same simulation parameters, include random motions, and are adaptively refined to the same maximum resolution ($\approx 3$ pc/cell).

We perform comparisons for simulations with either only radiative cooling or radiative cooling and isotropic thermal conduction at $f = 0.1$. We show the cold gas mass and mixed gas mass evolution for both in Figure 4.1, and we show a time series of the densities for the radiative cooling and thermal conduction runs in Figure 4.2. The 2D runs produce less cold gas than their 3D counterparts in both cases, consistent with the findings of other authors (Armillotta et al., 2016; Banda-Barragán, 2016; Grønnow et al., 2017). We also notice that 2D simulations underestimate the amount of mixed gas, as can be seen on the right panel of Figure 4.1. The 3D simulations are fully mixed ($M_{\mathrm{mixed}}/M_{\mathrm{cloud,\ t=0}} = 1$) after $60$ Myrs, whereas the 2D simulations are mixed at a fraction $M_{\mathrm{mixed}}/M_{\mathrm{cloud,\ t=0}} \approx 0.65$. The reason for this is that essentially, the 2D setup simulates flow around an infinite cylinder, as opposed to a sphere. As such, the effective surface area for the 2D setup is a one-dimensional ring, which is much smaller than in the 3D case (Grønnow et al., 2018). 2D simulations therefore underestimate mixing.

Qualitatively, the 2D and 3D cases are distinctly different. While mixing is underestimated in the 2D case, the destruction of the cloud seems to be faster as compared to
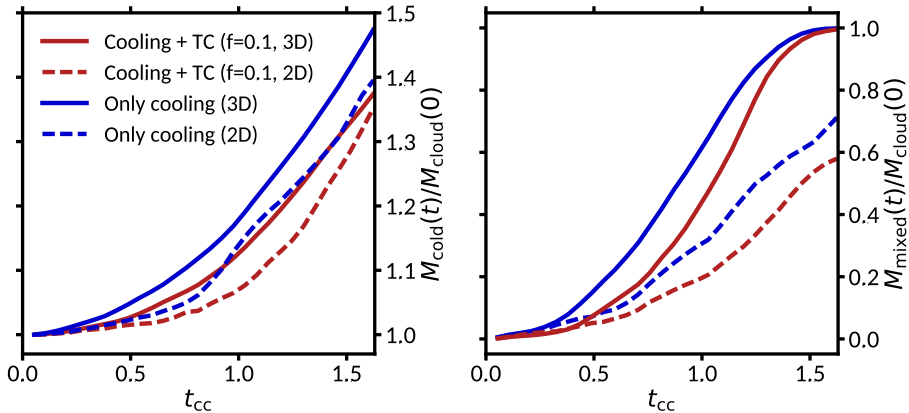
*Figure 4.1: The cold gas mass evolution for simulations with either only radiative cooling (blue) or radiative cooling and thermal conduction at $f = 0.1$ (red), as compared between 3D and 2D simulations (left). On the right, we show the evolution of the mixed gas mass over time. The colors and linestyles correspond to the same simulations as shown in the left panel. The evolution of the systems are shown as a function of the cloud-crushing time (Eqn. 3.8).*

the 3D case (Figure 4.2). The 2D geometry forces the ram-pressured material outwards, leading to an extended cloud-front that is rapidly destroyed. This does not happen in the 3D case, where the ram pressured material is not limited by the 2D geometry.

Overall, it is clear that a 2D geometry produces significantly different results both qualitatively and quantitatively. As such, to obtain reliable results from cloud-wind simulations a fully 3D simulation setup is desirable.

## 4.2 Turbulence & Cloud Stability

As mentioned in Chapter 3.2, we have introduced turbulence in the cloud in the form of initial random motions of $\approx 10$ km/s. In this section we consider the effect of this turbulence on the cloud stability, and on the diagnostics as described in Section 3.3.

Turbulence is added to the cloud ($r < r_0$) with Mach-numbers $\mathcal{M} \approx 1$. To make sure these velocities still produce a stable cloud that does not fall apart, we perform a simple simulation where there is no relative velocity between the cloud and the halo. We perform these static cloud simulations for i) an adiabatic setup (no added physics), ii) with only radiative cooling, and iii) with radiative cooling and thermal conduction at $f = 0.1$. The temperature distribution after 60 Myrs is shown in Figure 4.3. We notice that the cloud is stable against destruction by the turbulent velocities, as long as radiative cooling is included. When radiative cooling is included, any mixed material is quickly cooled down to lower temperature which causes the pressure to fall. This drop in pressure makes the cloud stable against mixing with the hot halo. These static cloud simulations furthermore show that the cloud can survive almost intact for at least 60 Myrs in a hot medium, even with the inclusion of thermal conduction.

Additionally, turbulence requires a random seed to be set, and will generate different random values for different seeds. In chaotic systems such as the cloud-wind problem, this might affect the values of certain diagnostics such as the cold gas mass evolution or the
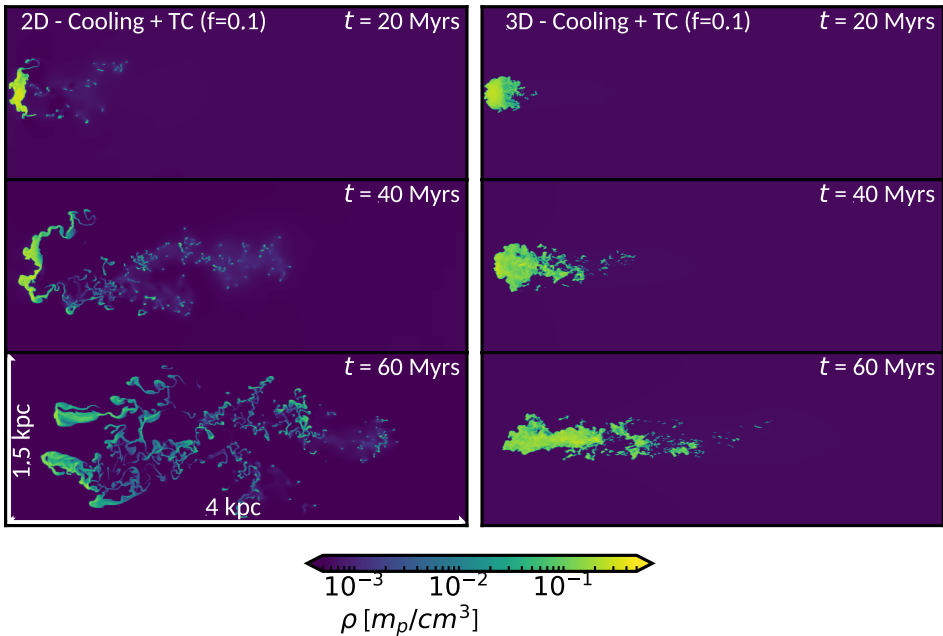
*Figure 4.2: The evolution of the density over time for the simulations including radiative cooling and isotropic thermal conduction at $f = 0.1$. We show the 2D simulation on the left, and the 3D simulation on the right. For the 3D simulations we show the projected density.*

mixing fraction. To check the extent of this, we have run the same simulation 5 times with a different random seed for each. We have done this for the simulation setup containing only radiative cooling, since this setup is likely to be most affected by this due to the lack of diffusive processes, and because these are relatively computationally cheap. We show the evolution of the cold gas mass and the mixed gas mass evolution in Figure 4.4. In general, the evolution of the cold gas mass and the mixed gas mass follow each other very closely. After 60 Myrs, the difference between the fiducial random seed and the outliers is about $\sim 5\%$ in terms of the cold gas mass. In terms of the mixing fraction there is no significant difference. It is unclear to what extent this affects simulations with thermal conduction or magnetic fields. However, considering that both thermal conduction and magnetic fields have been shown to suppress KH instabilities, the effect is likely smaller.
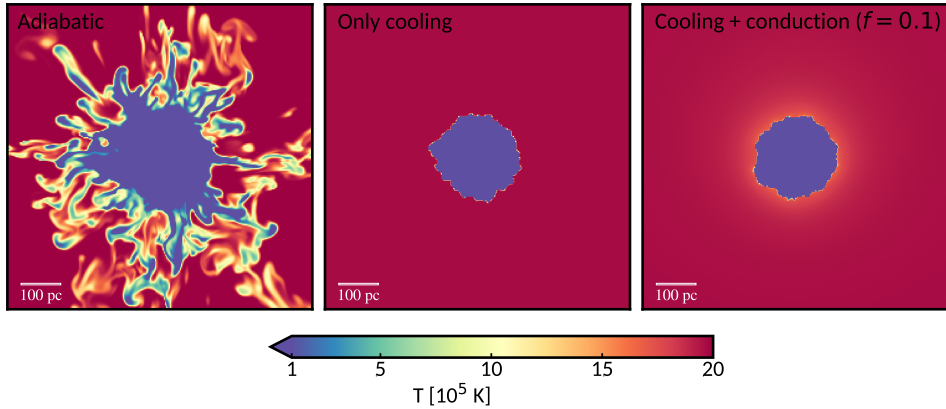
*Figure 4.3: Slices of the temperature through the simulation domain after $t = 60$ Myrs. We show the results for a simulation without any added physics (adiabatic, left), with radiative cooling (center), and with cooling and conduction (right). In these simulations there is no relative velocity between cloud and halo. The deformations shown are due to the turbulent velocities that are added to the cloud at initialisation, and are clearly quenched by the pressure confinement in the presence of radiative cooling.*
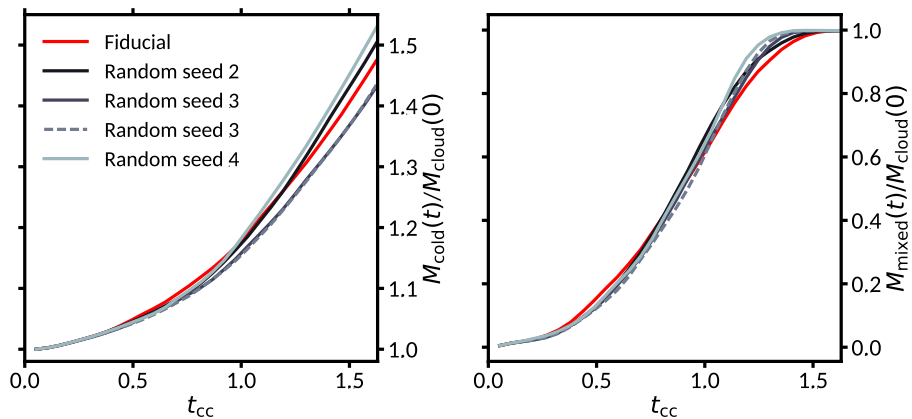


*Figure 4.4: An evaluation of the effects of different random seeds on the evolution of the cold gas mass in the case of only radiative cooling. We show the run used for our analysis in red, and 4 other simulations with different random seeds in shades of gray.*

# Chapter 5

# Scientific Results

In this chapter we present the main scientific results obtained through our HD and MHD simulations. We start with our fiducial simulation setup as described in Section 3.2, that is for a typical IVC with parameters in Table 3.1. After this we show the results that include the parameter variation as described in Section 3.2, with parameters in Table 3.2. Finally we show results for two special magnetic field setups: the tangled magnetic field and the oblique magnetic field.

## 5.1 Fiducial simulation setup

### 5.1.1 HD simulations

We investigate the effects of isotropic thermal conduction in 3D HD simulations by varying the efficiency of conduction through the $f$-factor. We show slices of the temperature distribution through part of the simulation domain after 60 Myrs in Fig. 5.1. Similar to previous work, e.g. Brüggen & Scannapieco (2016); Armillotta et al. (2016), we find that thermal conduction decreases the size of the wake through the evaporation of stripped cloudlets. The amount of cold gas in the simulation domain increases (i.e. there is condensation) in all cases, which is displayed in Fig. 5.2, top panel. However, the amount of condensation decreases with stronger (higher value of $f$) thermal conduction. Additionally, we show the mixed gas evolution in Fig. 5.2, bottom panel. All runs except $f = 0.2$ are fully mixed ($M_{\text{mixed}}/M_{\text{cloud, t=0}} = 1$) after 60 Myrs. This noticeable decrease in mixing efficiency for the $f = 0.2$ run shows that thermal conduction can have an additional effect, on which we expand later in this section.

According to the work by Begelman & McKee (1990), the thermal instability is suppressed on scales smaller than the Field length $\lambda_{\text{F}}$, named after the work on thermal instability by Field (1965):

$$\lambda_{\text{F}} = \sqrt{\frac{f \kappa_{\text{Sp}} T_{\text{hot}}}{n_{\text{cold}}^2 \Lambda(T_{\text{cold}})}}, \tag{5.1}$$

where $n_{\text{cold}}$ is the number density of cold (in our case $\sim 10^4$ K) material, and $\Lambda(T_{\text{cold}})$ is the cooling rate at this temperature[1]. For our fiducial simulations the Field length varies

---

[1] Since we implement a cooling floor at $T = 10^4$ K, in principle there is no cooling at this temperature. Instead, we take the cooling rate slightly above $10^4 K$ and take $\Lambda(T_{\text{cold}}) = 10^{-24}$ ergs cm$^3$/s.
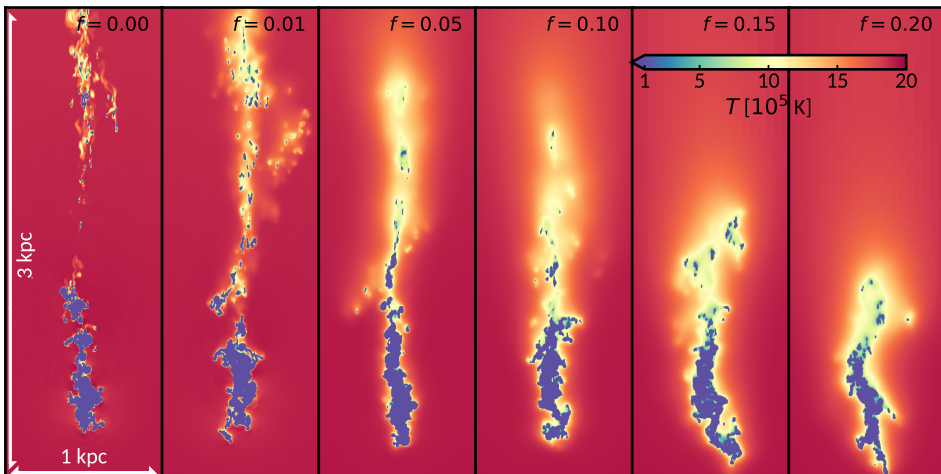
Figure 5.1: *Slices through part of the simulation domain of the gas temperature at $t = 60$ Myr for the fiducial simulation setup (Table 3.1). We vary the efficiency of isotropic thermal conduction with the $f$-factor from $f = 0.0$ (no thermal conduction) to $f = 0.20$ (strong thermal conduction) of the Spitzer value.*

in the range $\sim 10 - 60$ pc for $f = 0.01 - 0.20$, respectively. Hence, for weak thermal conduction ($f = 0.01$) the Field length is slightly below the size of ablated cloudlets ($\sim 10$ pc) and they do not evaporate. However, stronger thermal conduction increases the Field length and thus quickly dominates over cooling. We also see the formation of a smooth, intermediate temperature wake. Ablated cloudlets inside this intermediate temperature wake are more stable against evaporation since $T_{\mathrm{hot}}$ is smaller, which decreases the Field length. It is for this reason that some cloudlets are seen to survive in the wake even for strong ($f = 0.2$) thermal conduction. Note also that in the strong thermal conduction cases ($f = 0.15 - 0.2$), the Field length is $\approx 50$ pc, which evidently has a strong effect on the evolution of the cloud itself. We argue that in this case, thermal conduction can form and maintain a smooth temperature gradient between the head of the cloud and the hot halo. This subsequently creates a less steep density gradient that can suppress the formation of KH-instabilities (Vieser & Hensler, 2007), which extends the lifetime of the cloud (Armillotta et al., 2017).

Therefore the primary effect of thermal conduction is the evaporation of ablated cloudlets. However, in cases where thermal conduction is very strong, a secondary effect comes in that suppresses KH instabilities and delays mixing and condensation.

### 5.1.2 MHD simulations

We perform MHD simulations with and without anisotropic thermal conduction, and we show temperature slices for a weak (0.1 $\mu$G), magnetic field perpendicular to the motion of the cloud ($B_x = B_z = 0$, and $B_y = B_0$) in Figure 5.3. The magnetic field is sufficiently strong even in the weak field setup that the dynamical evolution of the system is affected by the magnetic field. By a magnetic draping effect (Dursi & Pfrommer, 2008; Grønnow et al., 2018), field lines are swept up and stretched by the cloud leading to significant field amplification as we show in Figure 5.4. Magnetic pressure becomes dynamically important and squeezes cloud material along one axis, see e.g. the top panels of Figures 5.3 and
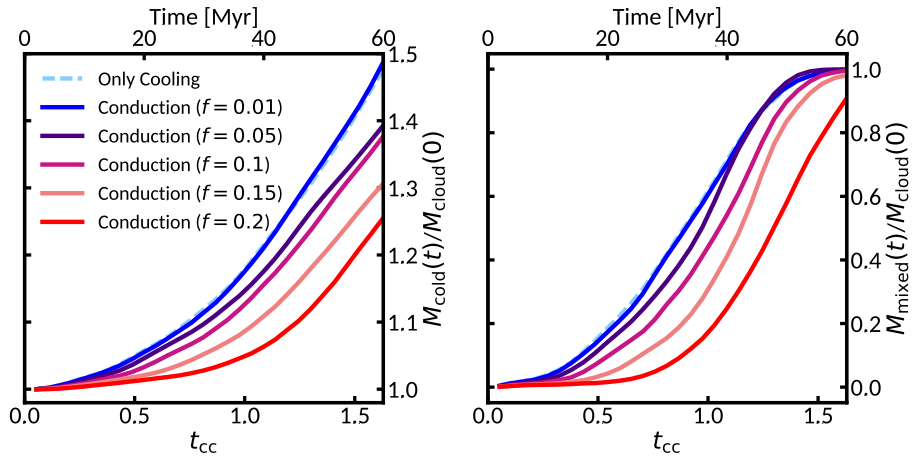
Figure 5.2: *We show the cold gas mass evolution (left) for our fiducial simulation setup (Table 3.1) for HD runs. We vary only the efficiency of isotropic thermal conduction through the parameter $f$. On the right, we show the mixing fraction for the same simulations, where the color coding is the same as for the left panel.*
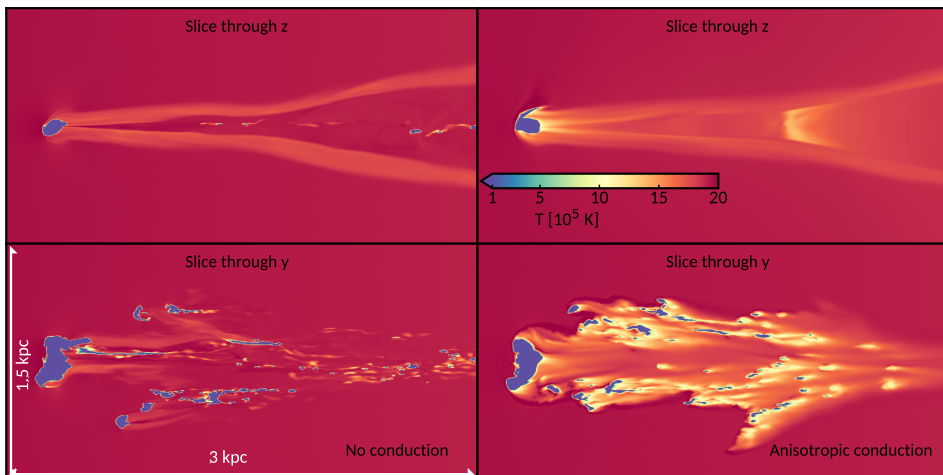


Figure 5.3: *Slices through part of the simulation domain of the temperature in the weak, perpendicular magnetic field runs for our fiducial simulation setup (Table 3.1). To illustrate the anisotropic morphology we show slices through the y- and z-axes. The magnetic field is initially parallel to the y-axis. We show the simulation without thermal conduction on the left, and the simulation with anisotropic conduction on the right.*
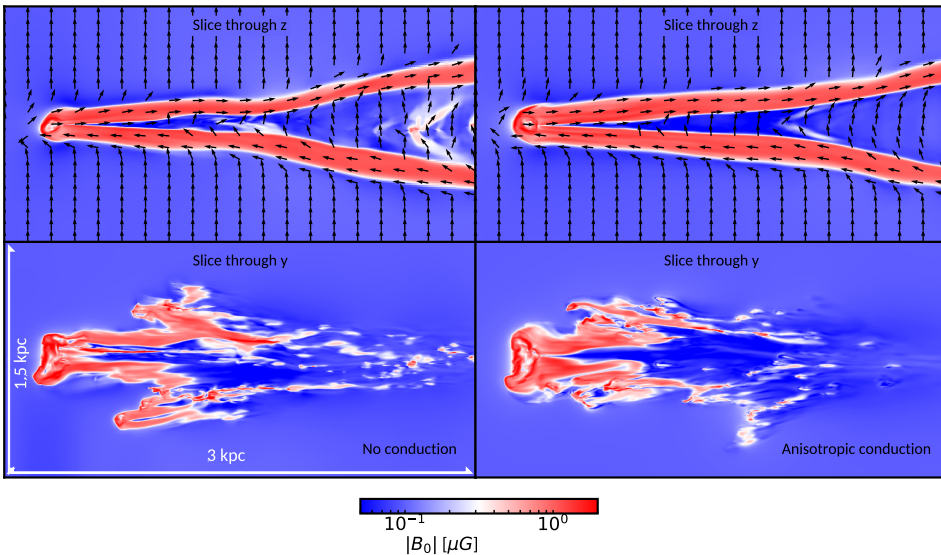
*Figure 5.4: The same simulations as shown in Figure 5.3, but now we show slices of the magnetic field strength (colors) and orientation (arrows). We overlay the normalised magnetic field vectors on the top panels. We do not include the field vectors in the bottom panels since the field is mostly oriented into the paper.*

5.4), which causes the cloud to expand along the axis perpendicular to it (bottom panels of Figures 5.3 and 5.4). The overall morphology of the cloud gas is not strongly affected by the inclusion of anisotropic thermal conduction in this case. However, we notice that thermal conduction creates a wake with temperatures of $T \approx 1 - 1.5 \times 10^6$ K. Due to the magnetic draping effect the field lines are wrapped around the head of the cloud and cloudlets. Since thermal conduction is only efficient along the field lines, a steep temperature gradient between cloud and hot halo can be maintained for at least 60 Myrs. Additionally, we notice that small ablated cloudlets can survive even with thermal conduction turned on, which is consistent with the findings of Liang & Remming (2020) in their 2D MHD simulations.

We show temperature and magnetic field slices with a weak field parallel to the motion of the cloud ($B_x = B_0$, and $B_y, B_z = 0$) in Figure 5.5. While the elongated morphology is more akin to the runs without a magnetic field, we notice that there is significantly less ablation in this case. The magnetic field efficiently suppresses KH instabilities (Sur et al., 2014), leading to a narrow wake and little ablation. In this case we notice a morphological change with the inclusion of thermal conduction. The magnetic field lines enter the cold cloud directly from the hot halo, leading to highly efficient thermal conduction at the cloud-halo interface. Similar to the HD setups with strong ($f = 0.15 - 0.2$) thermal conduction, this creates a temperature and density gradient at the cloud-halo interface. In this case, both the magnetic field and the temperature gradient act to suppress stripping by KH instability.

We show temperature slices of the simulation including a strong, perpendicular field in Figure 5.6, and slices of the magnetic field strength in Figure 5.7. We find that the strong perpendicular field splits up the cloud into multiple highly magnetised filaments, similar to the results of McCourt et al. (2015); Banda-Barragán et al. (2018); Cottle et al. (2020). These filaments are magnetically shielded from collapse. The strong field also
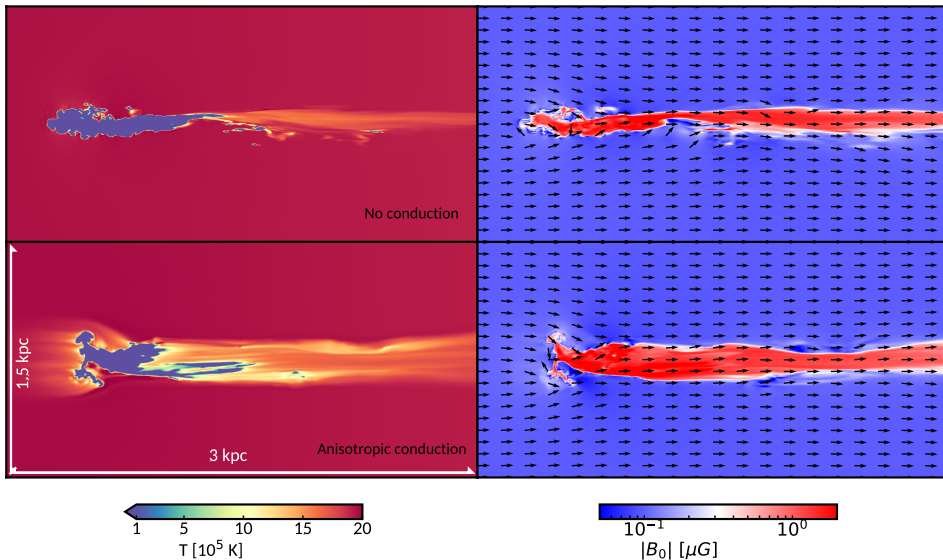
*Figure 5.5: Slices of a weak, parallel magnetic field without thermal conduction (top) and with anisotropic thermal conduction (bottom) for the fiducial simulation setup (Table 3.1). We show the temperature on the left, and the magnetic field strength (colors), and orientation (arrows) on the right.*

drapes around the cloud, but at a small angle due to its increased strength. The magnetic tension force due to the magnetic draping effect is proportional to $|\boldsymbol{B}|^2$, which is a factor 100 higher than for the weak field, and thus plays a big role in this simulation. This drag force due to the magnetic tension has caused the cloud to be nearly comoving with the hot gas after just 60 Myrs. Similar to the weak field, the morphology of the strong field run does not significantly change with the addition of thermal conduction. We do notice however, that anisotropic thermal conduction creates a thin region of intermediate temperature $T \approx 10^6$ K. We also notice thin filaments of $T \approx 1 - 1.5 \times 10^6$ K. These correspond to regions where the magnetic field strength is strongly amplified. The high magnetic strength decreases the density and temperature of the gas. These filaments in a simulation with a strong, transverse field are also seen in e.g. McCourt et al. (2015).

We only briefly mention the strong parallel field setup, since we expect that numerical instabilities could have affected the evolution of the system. We find that a bubble shaped region of low magnetic pressure forms ahead of the cloud. Strong parallel field setups are not commonly performed in the literature. However, we can compare to Cottle et al. (2020), who have performed their simulations with a $\mathcal{M} \approx 3.5$ wind, which is approximately 1700 km/s. They show slices of the density and the plasma-$\beta$ parameter, which we also show in Figure 5.8. We notice that while the density shows a similar evolution, with thin, strongly magnetised flux ropes, the plasma-$\beta$ parameter shows a deviation which is not seen in the work of Cottle et al. (2020). It is unclear whether this deviation arises from numerical instability, or due to a physical phenomenon. As such, we do include these simulations in our analysis, but make no conclusions based on these results.

We show the cold gas evolution for all magnetic field setups in Fig. 5.9. As found previously by Grønnow et al. (2018), we notice that all field setups have less condensation than the HD 'only cooling' run (as shown in Figure 5.1). In the perpendicular field setups the condensation is further decreased by $\sim 10\%$ when thermal conduction is included.
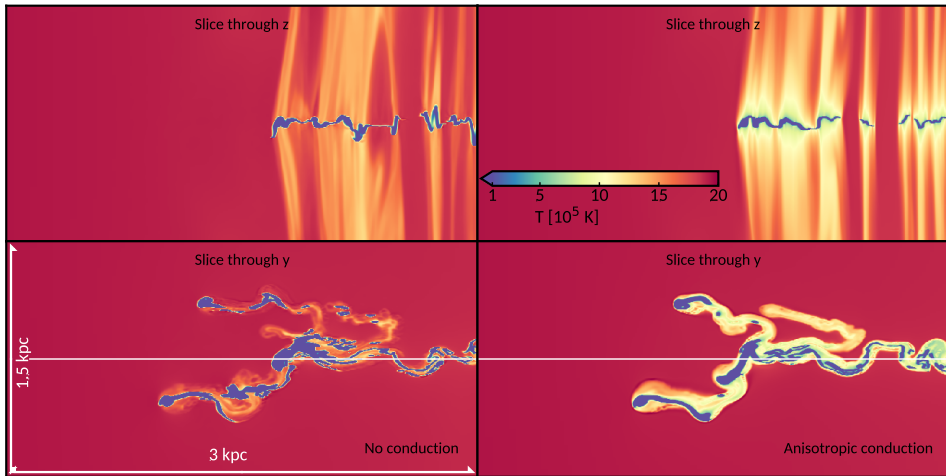
*Figure 5.6: Temperature slices after* 60 *Myrs through the simulation domain for the strong, per-pendicular field setup. Similar to McCourt et al. (2015); Banda-Barragán et al. (2017); Cottle et al. (2020) we find that a strong magnetic field can form highly magnetized filaments, that can survive for long times. Also notice how the magnetic tension force has caused a drastic acceleration of the cloud material, which is nearly completely comoving with the wind after* 60 *Myrs. Note that these slices are through the centers of the simulation domain. The annotated white line in the bottom panels corresponds to where the slice is performed for the top panels. By following the annotated white line, one notices that these intermediate temperature regions are associated with the cold filaments. The thin filaments of intermediate temperature correspond to regions of high magnetic field strength (Figure 5.7).*
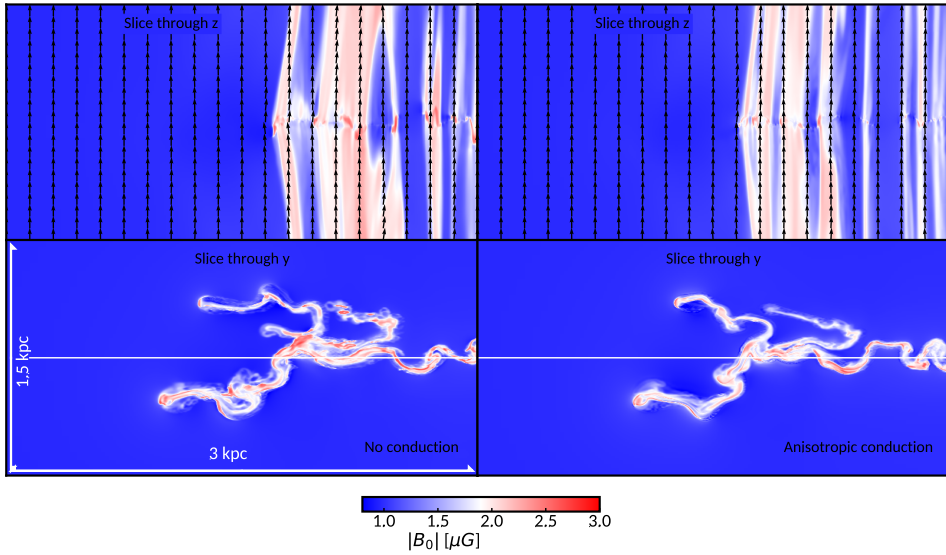
*Figure 5.7: The same simulations as shown in Figure 5.6, but now we show slices of the magnetic field strength (colors) and orientation (arrows). Note that the arrows are normalised. We do not include the field vectors in the bottom panels since the field is mostly oriented into the paper. Notice that the magnetic draping effect (as seen in the weak field, Figure 5.4) is not seen in the strong field. We annotate the same white line as in Figure 5.6 in the bottom panels which indicates where the slice is performed in the top panels. Notice in the top panels that the regions of high magnetic field strength correspond to the intermediate temperature regions in Figure 5.6.*
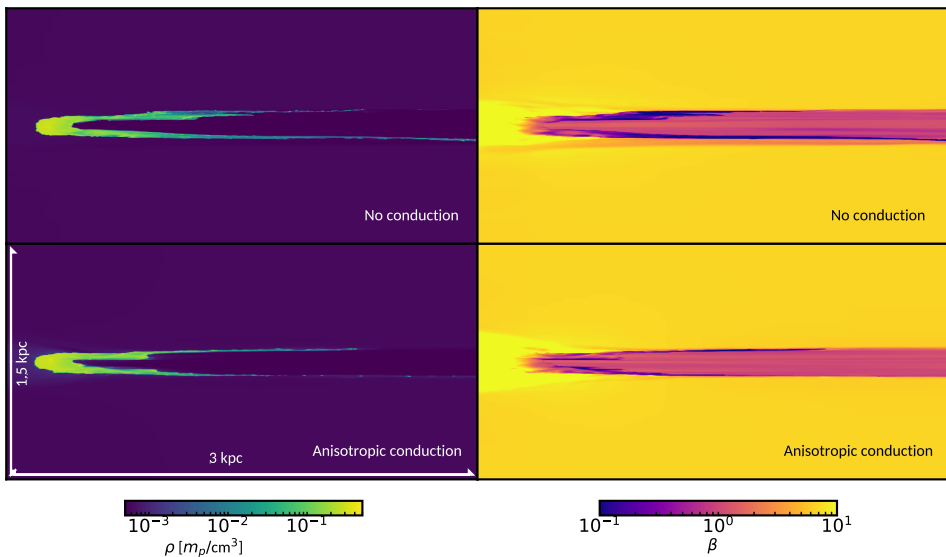


*Figure 5.8: On the left, we show slices through the density after 60 Myrs for the strong, parallel field setup. We show the runs without conduction in the top panels, and with anisotropic thermal conduction in the bottom panels. On the right panels, we show the plasma-$\beta$ parameter. Notice that the thin filaments are highly magnetised ($\beta < 1$). Furthermore, notice the region in front (to the left in the plot) of the cloud that has a higher value for $\beta$.*
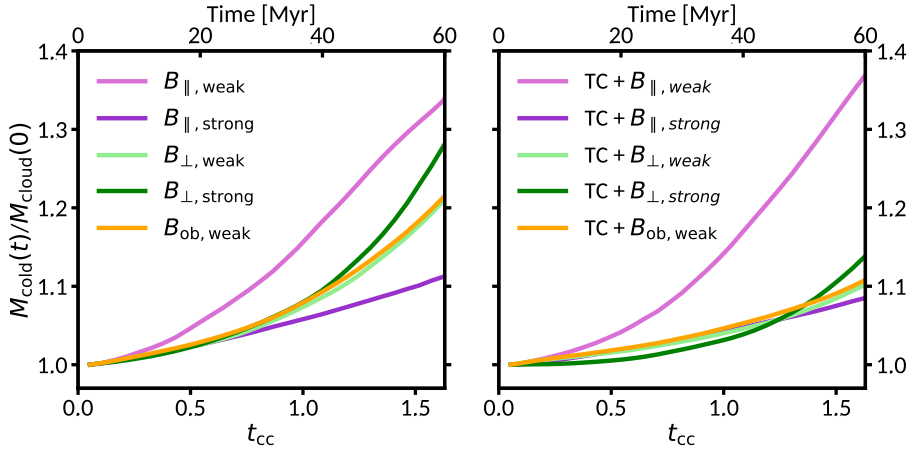
Figure 5.9: The cold gas evolution for our fiducial MHD simulation setup runs with thermal conduction turned off (left), and for runs with anisotropic thermal conduction (TC) turned on (right). The different curves refer to different strengths & orientations of the magnetic field. Note that all simulations are run with radiative cooling.

Due to the magnetic draping effect thermal conduction does not operate efficiently on the cloud-halo interface, and ablation is mostly unhindered. Hence, the decrease in condensation is due to the evaporation of cloudlets in the wake. In contrast, for the parallel field setups the condensation changes little with the inclusion of thermal conduction. In this case the ablation from the cloud is already very limited due to the magnetic field orientation, such that evaporation of cloudlets is negligible. The dominant way for the cloud to condense material is thus directly onto the cloud, as opposed to in the wake. The figure also shows an oblique orientation of the field ($B_{ob}$, where $B_x = B_y = \frac{B_0}{\sqrt{2}}$, and $B_z = 0$) that we discuss in Section 5.6.

### 5.1.3 The efficiency of thermal conduction

The $f$-factor only approximates the suppression effect in the thermal conduction heat flux, so in order to isolate the effect of adding thermal conduction to the simulations we compare the ratio of cold gas masses as follows. We calculate

$$\Delta M_{HD} = \frac{M_{cold,\, HD}}{M_{cold,\, HD + conduction}},$$  (5.2)

for HD runs, and

$$\Delta M_{MHD} = \frac{M_{cold,\, MHD}}{M_{cold,\, MHD + conduction}},$$  (5.3)

for MHD runs. In this way, the majority of the difference in the cold gas mass between HD and MHD simulations that comes from the magnetic field hindering the KH instability is filtered out. With these ratios we can thus obtain an estimate of suitable values for $f$ by comparing the approximated suppression in HD simulations to the 'true' suppression in the MHD simulations.

In Figure 5.10, we show the results for Eqn. 5.2 on the left, and the results for Eqn. 5.3 on the right, for all simulation setups. The first row contains the results for the fiducial

simulation setup, seen until now. The results show percentage wise how much cold gas is formed by runs without thermal conduction, compared to runs with thermal conduction. We notice a clear distinction between field orientations, where as mentioned before, perpendicular fields are more strongly suppressed in terms of the cold gas formed than the parallel fields. For perpendicular magnetic fields we find that a thermal conduction efficiency of $f \approx 0.10 - 0.15$ fits well, and for parallel fields the effect of thermal conduction is near negligible at $f \approx 0.02$.

## 5.2 Varying cloud metallicity

Typically IVC's are observed to have metallicities close to solar (see e.g. Richter et al., 2001), indicating that their origin was likely close to the metal-rich galactic disc, and were possibly ejected by the galactic fountain process (Shapiro & Field, 1976; Bregman, 1980; Spitoni et al., 2008; Fraternali & Binney, 2006; Fraternali, 2017). However, some IVC's (see e.g. Hernandez et al., 2013; Fukui et al., 2018) show signs of sub-solar metallicity. Here we examine the effect of lowering the cloud metallicity to 10% solar. This can be more typical of HVC's (e.g. Wakker et al., 2007), which we also consider in Section 5.4.

It is well known that media with higher metallicity have a shorter cooling time than lower metallicity media, due to the rapid cooling by metal lines as compared to hydrogen and helium. However, this does not necessarily lead to a significant increase in condensation in "cloud-wind" systems. An increased cooling rate has been found, for instance, to suppress the stripping of cloudlets (Cooper et al., 2009). We also find that the cloudlets that are stripped and that mix with the halo gas do cool more efficiently, which in this case leads to very similar amounts of condensation, as can be seen in the left panel of Figure 5.11. We show the temperature distribution after 60 Myrs in Figure 5.12. When isotropic thermal conduction is included the runs with lower cloud metallicity produce significantly less cold gas than their higher metallicity counterparts. From the definition of the Field length (Eqn. 5.1), we know that a decrease in cooling rate increases the Field length. At the peak of the cooling curve ($T \sim 10^5$ K), the difference between solar and 10% solar can be up to a factor 10, which increases the Field length by a factor $\sqrt{10}$. This difference in cooling rate converges around $T = 10^4$ K, such that the overall change to the Field length is small, but not negligible. Thus, cloudlets are more prone to evaporate for the lower metallicity setup leading to less condensation. This can be seen clearly by comparing the $f = 0.20$ runs between Figures 5.1 and 5.12, where the latter shows no stripped cloudlets in the wake. In addition, the mixing fraction in the right panel of Figure 5.11, suggests that the mixing efficiency is also suppressed more strongly for a lower cloud metallicity.

We show the cold gas evolution for the MHD simulations with anisotropic thermal conduction in Figure 5.13 on the left panel, and the suppression effect in Figure 5.10, second row. The amount of cold gas formed is less than in the simulations with a solar metallicity cloud in all cases. The suppression effect in the MHD simulations is very similar to that in fiducial simulation setups. However, the suppression effect for the HD runs does change significantly, which suggests an overall value of $f \approx 0.05 - 0.10$, lower than what is found in the fiducial simulation case. For the 10% solar metallicity cloud setup we have also performed a "tangled" magnetic field simulation ($B_{\text{tang}}$), on which we expand in Section 5.5.

$$\Delta M_{\mathrm{HD}} = \frac{M_{\mathrm{HD}}}{M_{\mathrm{HD + conduction}}} \qquad\qquad \Delta M_{\mathrm{MHD}} = \frac{M_{\mathrm{MHD}}}{M_{\mathrm{MHD + conduction}}}$$
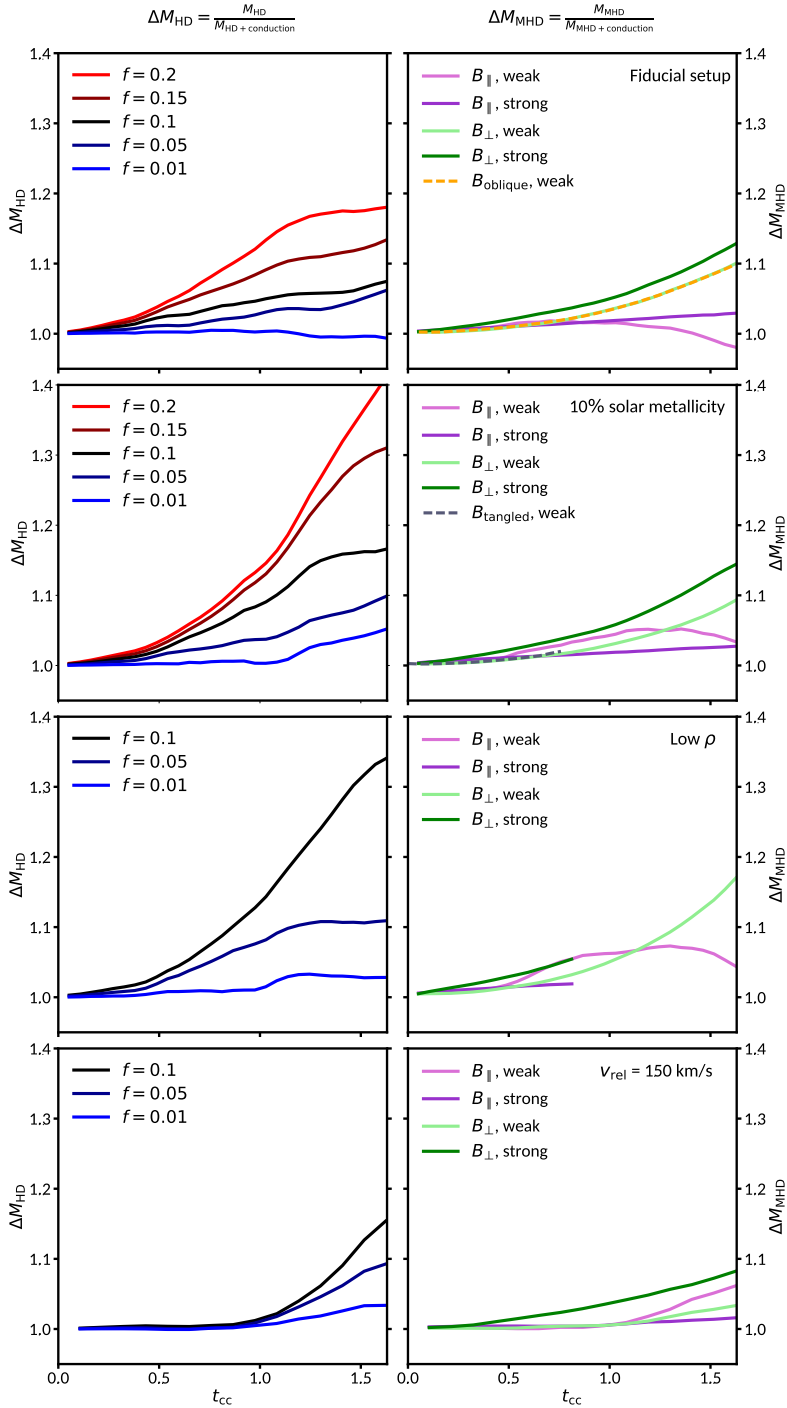


*Figure 5.10: We show the ratio of cold gas masses with and without isotropic thermal conduction for HD simulations at a certain $f$ (left), and for MHD simulations with anisotropic thermal conduction (right). Every row represents a different simulation setup. We show from top to bottom the fiducial, the 10% solar metallicity cloud, the lower density, and the high velocity setups, respectively.*
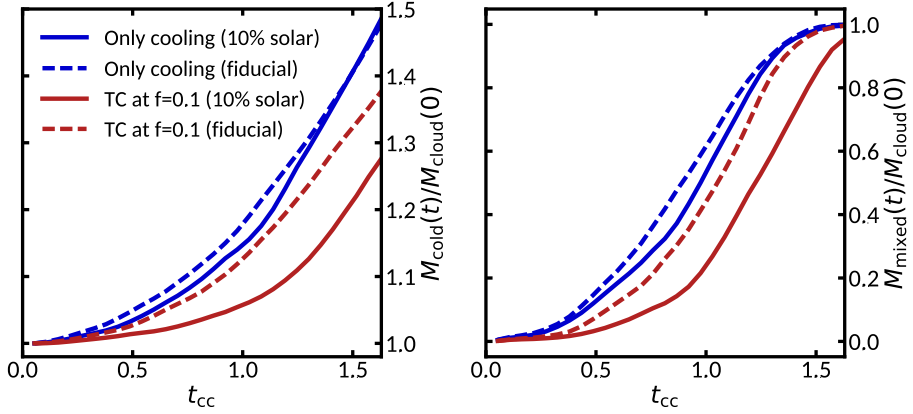
Figure 5.11: On the left panel we show the cold gas evolution as compared between a solar metallicity cloud (fiducial) and a 10% solar metallicity cloud. On the right panel we show the mixing fraction, where the colors and markers correspond to the same simulations as in the left panel.
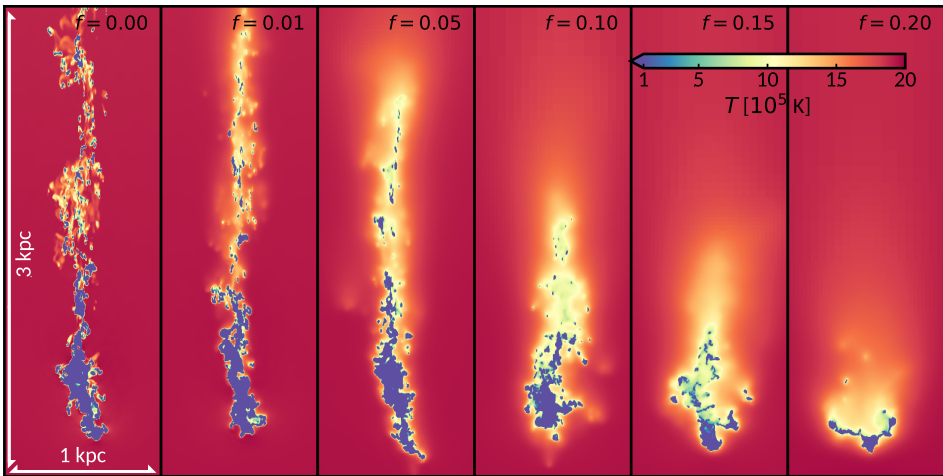


Figure 5.12: Slices through part of the simulation domain of the gas temperature at $t = 60$ Myr for the metal-poor cloud (10% solar metallicity) simulation setup. Similar to Figure 5.1, we vary the efficiency of isotropic thermal conduction with the $f$-factor from $f = 0.0$ (no thermal conduction, left) to $f = 0.20$ (strong thermal conduction, right) of the Spitzer value. These simulations are HD with isotropic thermal conduction and the values of $f$ are indicated on the top part of each panel.
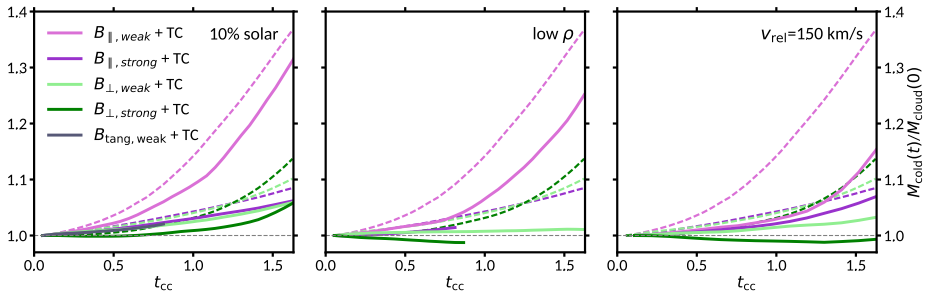
Figure 5.13: *Cold gas evolution for the non-fiducial simulation setups including radiative cooling, magnetic fields, and anisotropic thermal conduction (TC). From left to right we show the lower cloud metallicity setup, the lower cloud/halo density setup, and the higher velocity setup, respectively. In each panel we include the fiducial simulation results as dashed lines, where the colors correspond to the same magnetic field strength/orientation.*

## 5.3  Varying cloud and halo density

We investigate a factor-2 lower density for cloud and halo with $n_{\text{cloud}} = 0.1 \text{ cm}^{-3}$ and $n_{\text{hot}} = 5 \times 10^{-4} \text{ cm}^{-3}$. We keep the density contrast $\chi = \frac{n_{\text{cloud}}}{n_{\text{hot}}}$ at 200, such that the pressure equilibrium between cloud and hot halo is maintained without changing their temperatures. We show slices of the temperature for the HD simulations in Fig. 5.14. We make the same comparison between cold gas mass and mixing rate as for the lower metallicity setup in Fig. 5.15. Lowering the density has little effect on the simulations with only radiative cooling. Even though the cooling rate is proportional to $n^2$, it shows that the amount of condensation is likely limited by the mixing efficiency, as opposed to the cooling rate. However, with the inclusion of thermal conduction a drastic decrease in condensation is seen. For this reason we have not performed simulations with $f > 0.1$, since the condensation for $f = 0.1$ was already very small. For this lower density setup, the Field length increases by a factor 2. For $f > 0.1$ the Field length is of the order of the size of the cloud, which drastically alters its evolution. Besides rapid evaporation of any stripped cloudlets, there is another effect at play similar to the strong ($f = 0.2$) conduction runs of the fiducial setup. Qualitative examination shows that the cloud stays mostly intact over its full evolution time, with little to no stripping. The formation of KH instabilities is thus much more strongly suppressed than for the fiducial setup. The combined effect of less efficient cooling and a larger Field length is that condensation is near completely quenched for the simulation with thermal conduction at $f = 0.1$. Since we see similar effects for the simulation setup with lower metallicity, it could be possible that there is a turn-off point in parameter space where thermal conduction completely inhibits condensation.

In MHD simulations there is an additional effect as the plasma-$\beta$ parameter is now a factor 2 lower, which means that magnetic fields are more dynamically important. The combined effect of this, and less efficient cooling is clear: almost no condensation occurs in all field strengths and orientations except a weak, parallel field, as shown in the middle panel of Figure 5.13. We have run the strong field simulations for this setup until $\sim 0.8 t_{\text{cc}}$, due to numerical instabilities, likely associated with the dynamically important magnetic field. Since the strong field runs have shown a consistent trend in the other simulation setups, we argue that $0.8 t_{\text{cc}}$ gives a good indication of its behavior at $1.6 t_{\text{cc}}$. The simulation with a strong, transverse magnetic field is not only suppressed in condensation, but shows
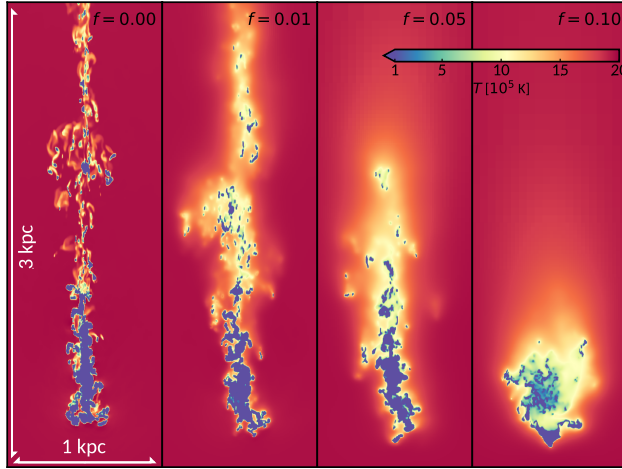
*Figure 5.14: Slices through part of the simulation domain of the gas temperature at $t = 60$ Myr for the lower density ($n_{\text{cloud}}$ and $n_{\text{hot}} = 0.1$ and $5 \times 10^{-4}$ cm$^{-3}$, respectively) simulation setup. We vary the efficiency of isotropic thermal conduction with the $f$-factor from $f = 0.0$ (no thermal conduction, left) to $f = 0.10$ (intermediate thermal conduction, right) of the Spitzer value.*
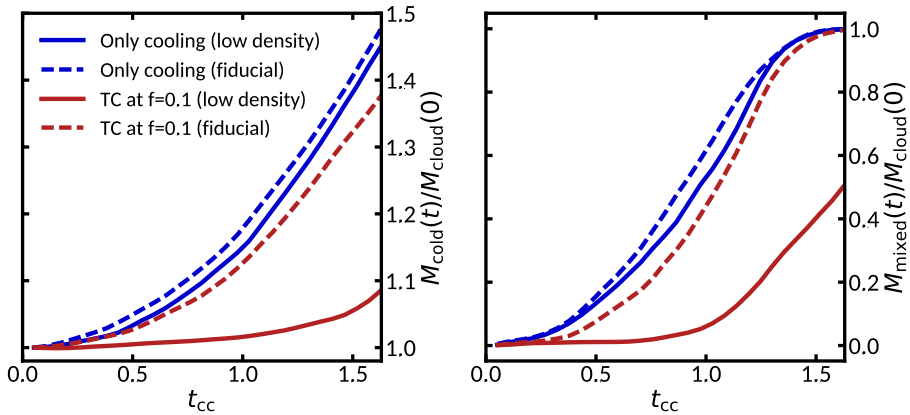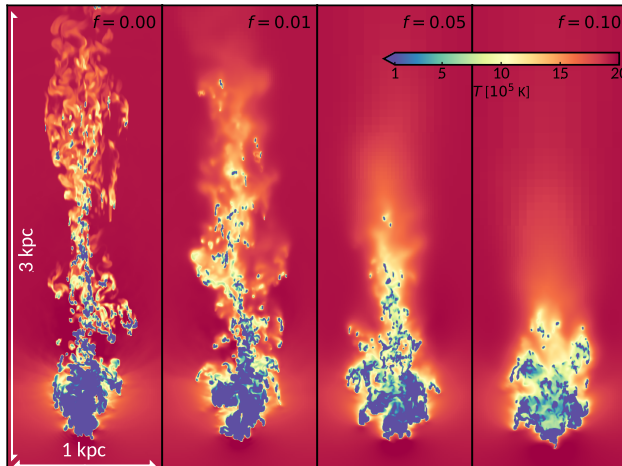


*Figure 5.15: Cold gas evolution (left) and the mixing fraction (right), as compared between the fiducial simulation setup and the low-density ($n_{\text{cloud}} = 0.1$ cm$^{-3}$, $n_{\text{hot}} = 5 \times 10^{-4}$ cm$^{-3}$) setup.*

*Figure 5.16: Slices through part of the simulation domain of the gas temperature at $t = 60$ Myr for the high velocity ($v_{\rm rel} = 150$ km/s) simulation setup. Similar to Figure 5.14, we vary the efficiency of isotropic thermal conduction with the $f$-factor from $f = 0.0$ (no thermal conduction, left) to $f = 0.10$ (intermediate thermal conduction, right) of the Spitzer value.*

a decrease in cold gas mass with time (evaporation).

Similar to the 10% solar metallicity setup, the efficiency of thermal conduction is lower as compared to the fiducial setup. In this case the suppression effect due to thermal conduction is stronger for both the HD and MHD runs (Figure 5.10, third row). We find for the lower density setup that perpendicular magnetic fields can be approximated with a thermal conduction efficiency of $f \approx 0.05 - 0.10$. For the parallel weak field, $f \approx 0.01$.

## 5.4 Varying relative velocity

In- or out-flowing gas clouds have been observed to have a wide range of velocities (e.g. Wakker et al., 2007), and a typical distinction is made between IVC's with typical galactic fountain velocities of $< 100$ km/s (Fraternali & Binney, 2008; Marasco et al., 2012) with respect to the disc gas, and HVCs with higher velocities. To some extent, we can consider this distinction valid also for relative velocities between clouds and a hot halo (Marinacci et al., 2011; Pezzulli & Fraternali, 2016; Tepper-García et al., 2019). We assess the effect of the relative velocity on the evolution of our clouds by increasing it to 150 km/s ($\mathcal{M} \approx 0.70$). Cloud-wind simulations with higher Mach numbers are generally harder to run numerically, but their evolution is also faster. Note that $t_{\rm cc}$ is a factor 2 smaller for this HVC setup, thus these simulations are performed until $t = 30$ Myrs. We show slices of the temperature in Fig. 5.16, and the cold gas mass evolution and mixing fractions for HD simulations in Figure 5.17. Note that similar to the lower density setup we have not performed HD simulations with $f > 0.1$ since the condensation for the $f = 0.1$ simulation was already very small. There is a substantial delay in the onset of condensation for the high-velocity setup. This is due to increased adiabatic heating, as shown in Grønnow et al. (2018).

For the MHD simulations, we show the suppression effect in Figure 5.10 on the fourth row, and the cold gas evolution in Figure 5.13 on the third row. In terms of the cloud-crushing time, we notice that there is a significant delay in the typical exponential growth
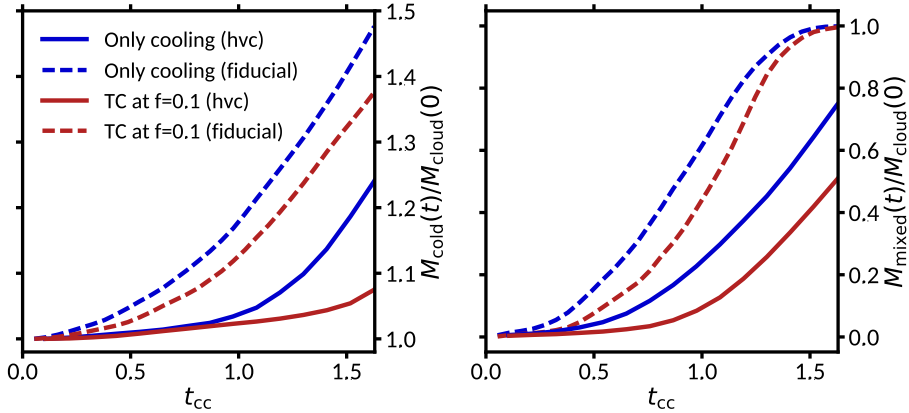
*Figure 5.17: Cold gas mass evolution (left) and mixing fraction (right) for a HVC ($v_{\rm rel} = 150$ km/s) as compared to the fiducial setup. Note that $t_{\rm cc}$ is a factor 2 smaller in this HVC setup with respect to the fiducial case.*

rate of cold gas seen in other simulation setups (see also Fraternali et al., 2015). Even after $1.6t_{\rm cc}$ the simulation with a strong, transverse magnetic field shows a net decrease in the amount of cold gas (evaporation). However, after $\approx 1.2t_{\rm cc}$ this seems to increase again indicating that condensation is not indefinitely suppressed.

For the high velocity setup, we also show the strong, parallel field in Figure 5.18. We recall from Section 5.1, that the strong, parallel field setup showed regions of low magnetic pressure ahead of the cloud which have not been previously found in the literature. In the high velocity cloud setup, we do not see this effect.

## 5.5 Tangled Magnetic Fields

It is expected that the magnetic field in galaxies has a large scale regular component, with a small scale turbulent component (Jansson & Farrar, 2012; Beck et al., 2016). Since thermal conduction is highly anisotropic in magnetic fields (see Section 2.4), a turbulent magnetic field could have important consequences for the efficiency of thermal conduction. In this section we describe our attempt to include a fully tangled magnetic field in our simulations.

### 5.5.1 Field Generation

In order to achieve an approximate equilibrium situation of a magnetic field that is not uniformly distributed, we will need to construct a force-free magnetic field. A force-free field has the advantage that it does not introduce Lorentz forces, and thus turbulence in the hot halo gas. The simulation setup therefore remains very similar to that described in Section 3.2.

The condition that no Lorentz force (see Eqn. 2.12) arises anywhere in the simulation domain, means that

$$\boldsymbol{F}_{\rm Lorentz} = \frac{1}{c}\boldsymbol{j} \times \boldsymbol{B} = (\boldsymbol{\nabla} \times \boldsymbol{B}) \times \boldsymbol{B} = 0. \tag{5.4}$$
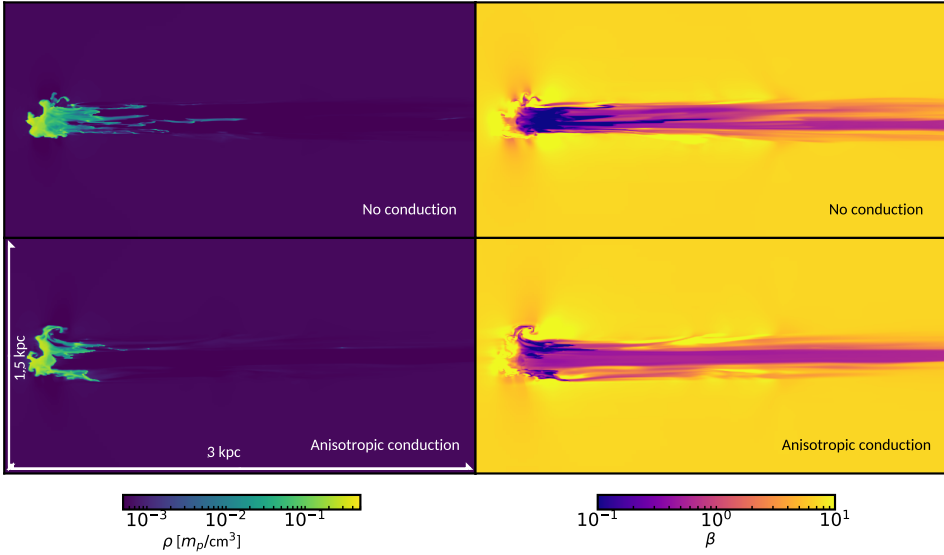
*Figure 5.18: On the left, we show slices through the density after 30 Myrs ($t = 1.6t_{cc}$) for the strong, parallel field setup in the HVC simulations with $v_{rel} = 150$ km/s. We show the runs without conduction on the top panels, and the runs with anisotropic thermal conduction on the bottom panels. On the right panels, we show the plasma-$\beta$ parameter.*

For our initial conditions the gravitational and plasma pressure gradients are zero, because we do not include gravity and we assume pressure equilibrium throughout the simulation domain. This leads to the simplified condition of

$$\nabla \times \boldsymbol{B} = \alpha(\boldsymbol{r})\boldsymbol{B}, \tag{5.5}$$

where $\alpha(\boldsymbol{r})$ is the correlation length, and is in general a function of position $\boldsymbol{r}$. If $\alpha$ is constant, then Eq. 5.5 becomes linear in $\boldsymbol{B}$ and the resulting field is called a linear force free field (LFFF). In this thesis I create a LFFF by a superposition of random modes of sine waves. This is done following the general method of van Ballegooijen & Cranmer (2010). In this method the magnetic field without any sort of boundary conditions can be written as a superposition of planar modes as

$$\boldsymbol{B}(\boldsymbol{r}) = \sum_{n=1}^{N} B_n[\hat{\boldsymbol{e}}_{1,n}\cos(\boldsymbol{k}_n \cdot \boldsymbol{r} + \beta_n) - \hat{\boldsymbol{e}}_{2,n}\sin(\boldsymbol{k}_n \cdot \boldsymbol{r} + \beta_n)], \tag{5.6}$$

where $\boldsymbol{r}$ is a position, $n$ is the current mode, $N$ is the total amount of modes, $B_n$ is the mode amplitude, $\beta_n$ is the phase angle, $\boldsymbol{k}_n \equiv \alpha\hat{\boldsymbol{e}}_{3,n}$ is the wavevector, and $[\hat{\boldsymbol{e}}_{1,n}, \hat{\boldsymbol{e}}_{2,n}, \hat{\boldsymbol{e}}_{3,n}]$ is a right handed and mutually orthogonal coordinate system given as

$$\hat{\boldsymbol{e}}_{1,n} = \cos\theta_n(\cos\phi_n\hat{\boldsymbol{y}} + \sin\phi_n\hat{\boldsymbol{z}}) - \sin\theta_n\hat{\boldsymbol{x}}, \tag{5.7}$$

$$\hat{\boldsymbol{e}}_{2,n} = -\sin\phi_n\hat{\boldsymbol{y}} + \cos\phi_n\hat{\boldsymbol{z}}, \tag{5.8}$$

$$\hat{\boldsymbol{e}}_{3,n} = \sin\theta_n(\cos\phi_n\hat{\boldsymbol{y}} + \sin\phi_n\hat{\boldsymbol{z}}) + \cos\theta_n\hat{\boldsymbol{x}}, \tag{5.9}$$

where $\theta_n, \phi_n$ are the direction angles of the current mode n. I choose an isotropic distribution of the direction angles i.e. $\phi_n$ is uniform over $[0, 2\pi]$ and $\cos\theta_n$ is uniform over $[-1, 1]$.
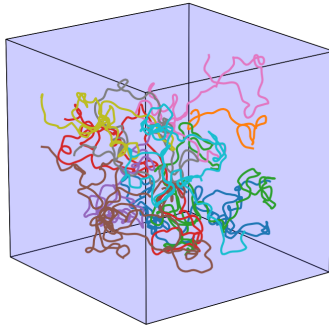
*Figure 5.19: Magnetic field lines in a realisation of a tangled magnetic field. The different colours correspond to different streamlines.*

Additionally, the phase angles are uniform in the range $[0, 2\pi]$. These choices make the ensemble average of the magnetic field $\langle \boldsymbol{B}_\beta(\boldsymbol{r}) \rangle = 0$. Furthermore, the root mean square (rms) value of the magnitude of the magnetic field is $|\boldsymbol{B}|_{\mathrm{rms}} = \frac{B_0}{\sqrt{N}}$. We show the magnetic field lines in a realisation of a tangled magnetic field as generated with the method described above in Figure 5.19.

The typical length scale of the turbulent mode is $l \approx \alpha^{-1}$. In our simulations $\alpha$ was set to $5/r_{\mathrm{cloud}}$, corresponding to $l = 20$ pc. This choice represents a trade-off between the turbulence length in the galactic magnetic field, and the ability to resolve the field that might interact with the cloud material. Estimates of the characteristic length scale of the turbulent mode of galactic magnetic fields are below 100 pc (e.g. Haverkorn et al., 2008; Beck et al., 2016). In our fiducial setup the turbulent lengthscale $l = 20$ pc corresponds to $\approx 7$ cells.

The tangled field is initialised at runtime, and is updated at the injection zone by calculating the magnetic field components at the new coordinate given by $x + t_{\mathrm{current}} \times v_{\mathrm{rel}}$. This ensures a smooth transition at the injection zone, such that the approximate force-free nature is conserved. However, in this case the outflow boundary conditions do not respect the force-free nature, and we expand on this in the following section.

### 5.5.2  Tangled results

In order to resolve the tangled magnetic field over the full simulation domain, the base level of refinement is increased from $[60 \times 20 \times 20]$ to $[480 \times 160 \times 160]$, and refined by a maximum of 2 levels. Slices through the temperature and magnetic fields are shown after 30 Myrs in Figure 5.20. Note that this is for the metal-poor cloud setup. Several issues have come to light for these simulations. As can be seen in Figure 5.20, the tangled field has lost pressure with respect to the beginning. We highlight this in a time series of the magnetic field in Figure 5.21, where we can see that the decay is already substantial after just 4 Myrs. The reason for this decay is likely a combination of the lack of boundary conditions for the field, and the finite resolution that can be used. The finite resolution could both cause spurious forces since the force-free approximation would be slightly violated,
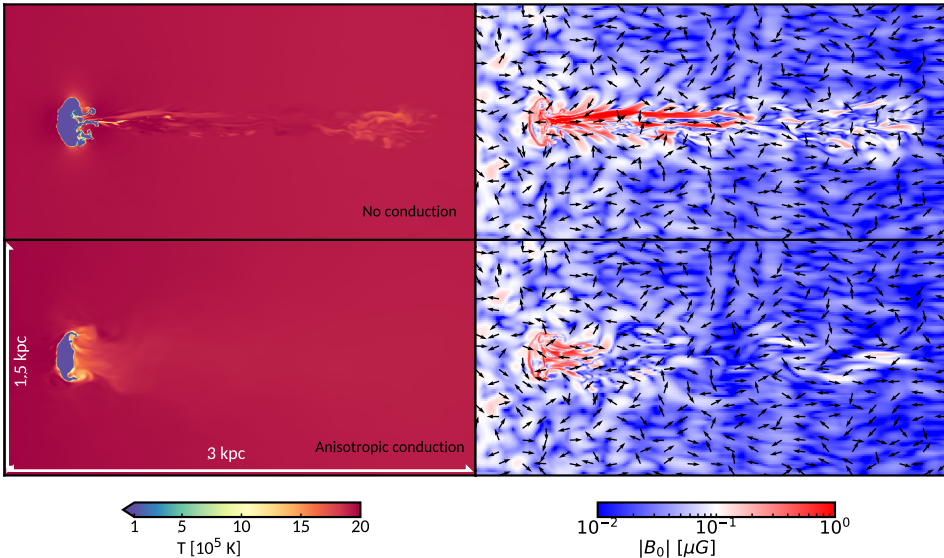
*Figure 5.20: Slices through the simulation domain at $t = 30$ Myrs of the temperature (left), and the magnetic field (right). We display the simulation without thermal conduction on the top panels, and the simulation with anisotropic thermal conduction on the bottom panels. We overlay the magnetic field vectors for the magnetic field plots to highlight their randomness.*

but it can also violate the solenoidal constraint ($\boldsymbol{\nabla} \cdot \boldsymbol{B} = 0$, see Section 2.2). The violation of this constraint can also induce spurious forces (e.g. Brackbill & Barnes, 1980). It might also be related to numerical resistivity, which can arise in ideal MHD simulations in arbitrarily aligned magnetic fields and can cause spurious, non-physical magnetic reconnection.

Another issue that came to light is the following. In AMR mode, the PLUTO code only provides an explicit solver for thermal conduction. This can result in a drastic timestep reduction in order to keep the required accuracy. While our other simulations including MHD and anisotropic thermal conduction had modest penalties to the maximum timestep (a factor 10-100 smaller than typical HD simulations), in this case the timestep was reduced by a factor $\sim 1000$ as compared to typical HD simulations. While we have run one simulation including radiative cooling, anisotropic thermal conduction, and a tangled magnetic field to 30 Myrs, it is unfeasible to run it for longer times.

Despite the aforementioned effects, it is clear that the tangled field drapes around the cloud (Figure 5.20, right). This behavior is similar to what happens in the perpendicular field setup, which suggests that the small scale turbulence in the CGM likely has only a small effect. It also suggests that the transverse field is the most probable field orientation that a cloud will experience, which we investigate further in Section 5.6.

Additionally we investigate whether this effect is purely due to low resolution effects in an ultra-high resolution ($15360 \times 5120$) 2D simulation. We show a short timeseries of the magnetic field in Figure 5.22. We notice that the decay in field strength is still present, which suggests that the resolution is likely not the problem. Therefore, the likely effect that causes the quick drop in field strength is the boundary conditions. There is no simple way to construct boundary conditions that ensure a force-free transition. However, van Ballegooijen & Cranmer (2010) also present a tangled field confined to a cylinder with force-free boundary conditions. Since PLUTO supports this geometry, this can be of interest to explore in future work.
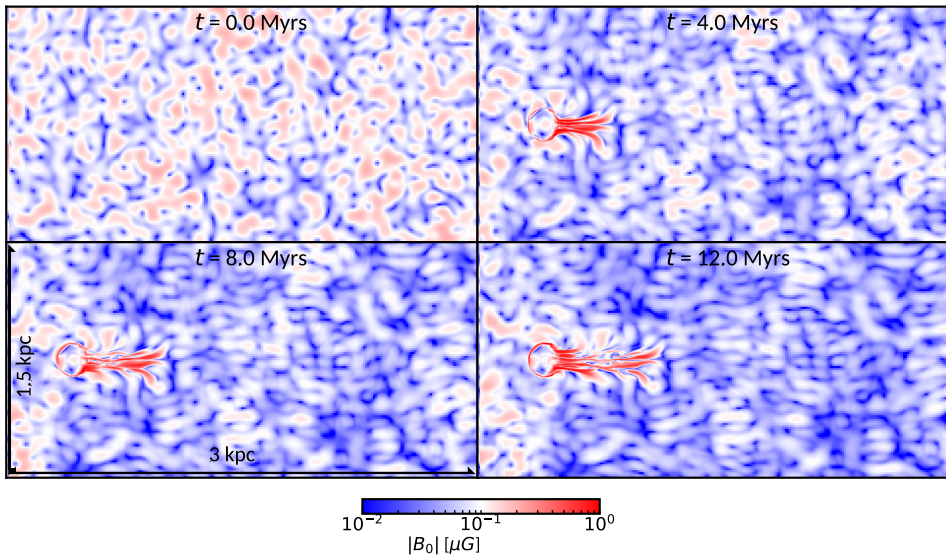
Figure 5.21: *Time evolution of the magnetic field in the case of a fully tangled field without thermal conduction. We notice that the magnetic field quickly evens out in < 6 Myrs.*
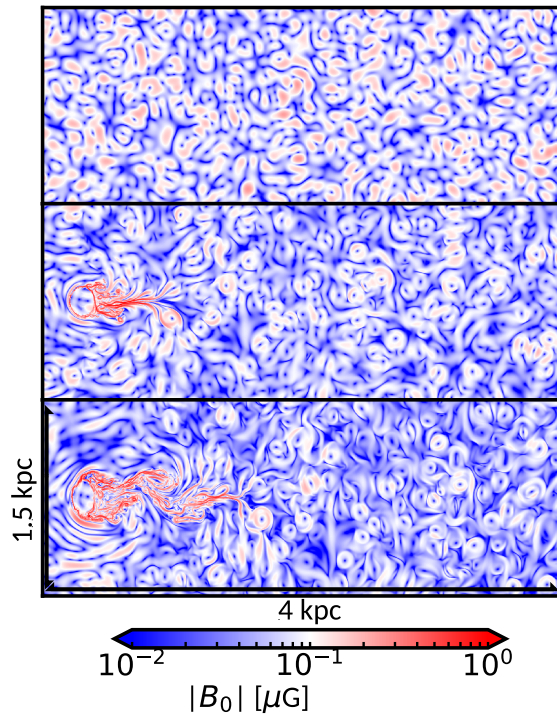


Figure 5.22: *A time series showing the magnitude of the magnetic field for an ultra high-resolution (15360 × 5120) 2D run of a tangled field. We show the initial conditions on the top panel, the simulation after t = 8 Myrs in the middle panel, and the simulation after t = 16 Myrs in the bottom panel. Note that the base level (the level at which the tangled field is resolved) without refinement is in this case 3840 × 1280.*
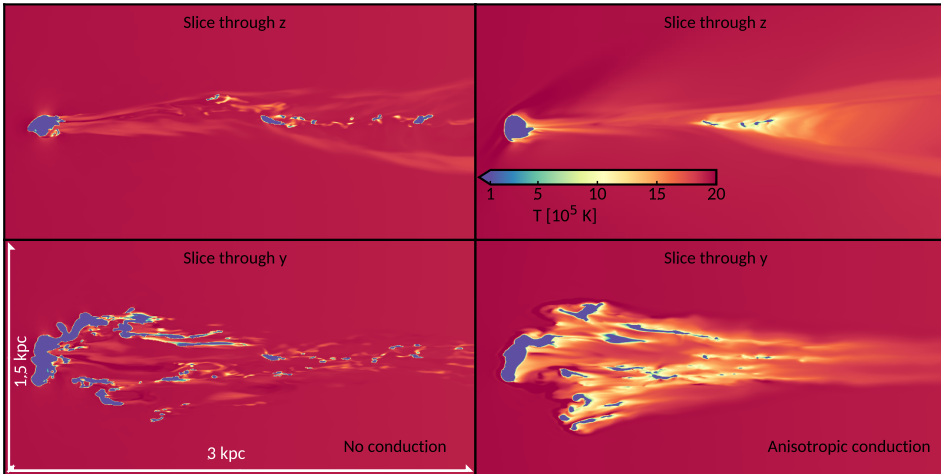
*Figure 5.23: Slices through the simulation domain of the temperature for the oblique magnetic field setup after $t = 60$ Myrs. We show the simulation without anisotropic thermal conduction on the left and with anisotropic thermal conduction on the right.*

## 5.6 Oblique Magnetic Field

So far, we have considered magnetic fields parallel ($B_\parallel$), and perpendicular ($B_\perp$) to the relative velocity, and a tangled magnetic field orientation. In this section we consider the effects of an oblique magnetic field, where $B_x = B_y = \frac{B_0}{\sqrt{2}}$, and $B_z = 0$. This field setup is thus in between $B_\parallel$ and $B_\perp$. Considering the expensiveness of the simulations including MHD and fully anisotropic thermal conduction, we only run this for the fiducial setup in the weak field case. We show the cold gas evolution in Figure 5.9, and the corresponding suppression effect in Figure 5.10. Additionally, we show slices of the temperature in Figure 5.23, and slices through the magnetic field in Figure 5.24. We notice that the evolution is very similar to the weak, perpendicular field setup, both in the cold gas evolution as well as the morphological evolution. The magnetic field drapes around the cloud, such that the cloud essentially experiences a magnetic field similar to the transverse magnetic field setup. The slightly higher condensation for the oblique field setup tells us that it does tend to the weak, parallel field case. In the strong field case there is no magnetic draping, and it is unclear if the oblique field setup will in this case also tend to the transverse field. We leave this exploration for future work.
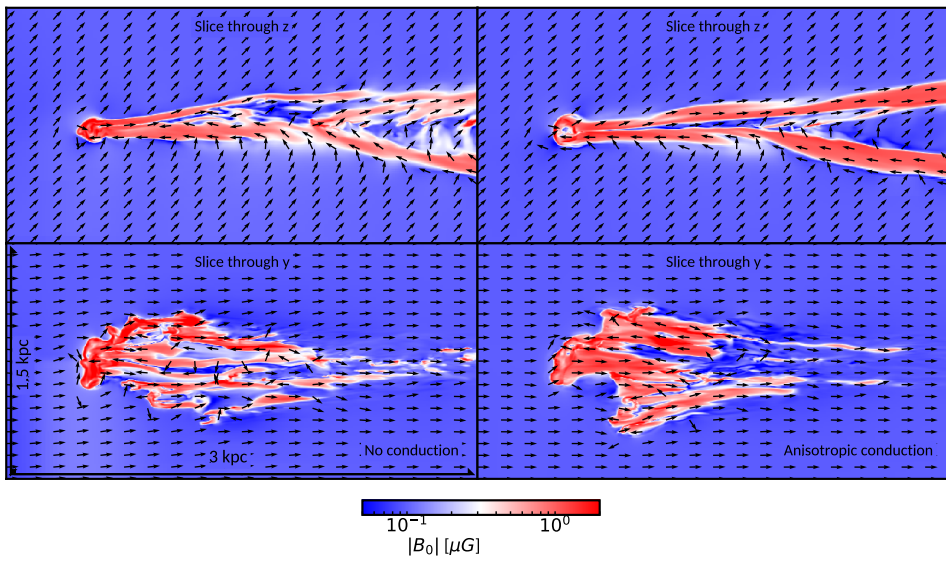
Figure 5.24: *The same as Figure 5.23, but for the magnetic field strength (colors) and orientations (arrows) for an oblique field.*

# Chapter 6

# Discussion

We have shown and compared the evolution of HD simulations with isotropic thermal conduction to MHD simulations with anisotropic thermal conduction. In particular, we have focused on the evolution of the cold gas mass (condensation). We isolated the effect of thermal conduction on the condensation by dividing the condensation of runs without thermal conduction by the condensation of runs with thermal conduction. We then used the resulting plots (Figure 5.10) to find the thermal conduction efficiency $f$ by direct comparison. We now show a summary plot of $f$ as a function of time where we have compared the real suppression from the MHD results to the approximate suppression from HD results in Figure 6.1. We show values after $\sim 0.8t_{cc}$ to allow the system to move away from its idealised initial conditions. To obtain these values we interpolate the MHD results to the curves in the HD results predicting a certain $f$. An upper limit of $f = 0.15$ seems to be valid for all simulations, consistent with the upper limit of $f = 0.20$ as found by Narayan & Medvedev (2001) for a tangled magnetic field. A clear dichotomy is also seen in different field orientations: perpendicular fields average to $0.07 \pm 0.04$, whereas parallel fields average to $0.03 \pm 0.02$. This is mainly due to the strongly suppressed stripping in the parallel field case as opposed to the perpendicular field, since thermal conduction can efficiently evaporate the stripped cloudlets. We find values for $f$ in the range 0.03-0.15 for the perpendicular field, and 0.01-0.06 for the parallel field setup. Despite the large spread, these values confirm that magnetic fields have an important effect in suppressing thermal conduction to $\lesssim 10\%$ of the Spitzer value. Below we discuss the effect resolution on our results and other potential limitations.

## 6.1 Convergence tests

We have verified for a subset of our simulations whether the results in terms of their cold gas mass evolution are converged. We perform full convergence tests for runs with only radiative cooling, radiative cooling and thermal conduction at $f = 0.1$, and for radiative cooling and a weak, transverse magnetic field. We have not run the convergence test for simulations with radiative cooling, thermal conduction *and* magnetic fields to 60 Myrs due to computational constraints.

It has been estimated that runs with only radiative cooling shatter into cold cloudlets with size $\sim 0.1\mathrm{pc}/n$, where $n$ is the number density (McCourt et al., 2018). These sub-parsec scales are far out of our reach in terms of computational power for 3D simulations. However, thermal conduction effectively evaporates these small scale instabilities
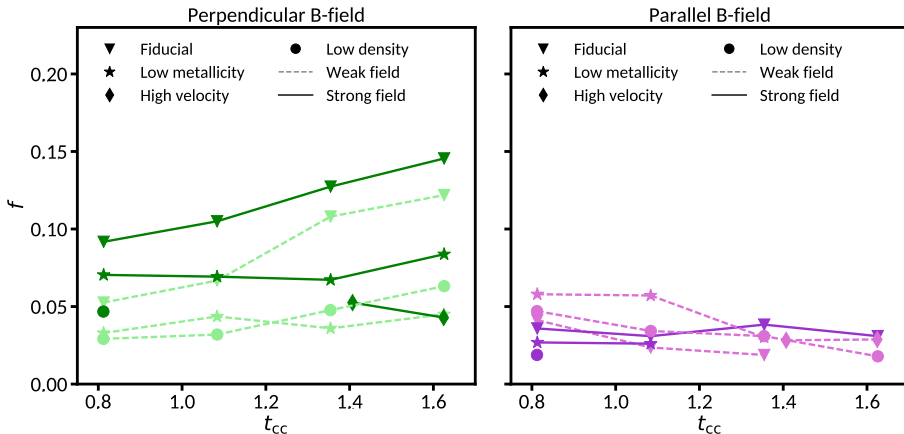
Figure 6.1: *Linearly interpolated values for the $f$-factor sampled at regular time intervals. We do not plot the first $\sim 0.8t_{cc}$ since the system needs time to avoid a bias from its idealised initial conditions. There is a clear dichotomy between perpendicular and parallel magnetic fields, where thermal conduction is much less efficient in the parallel field case.*

and hence the resolution necessary for convergence is likely more achievable, which was also noticed by Armillotta et al. (2016), their Figure 4. We show our resolution studies in terms of condensation in Figure 6.2, and in terms of density projections in Figure 6.3. Note that the turbulent velocities that were added to the cloud can affect the condensation by $\sim 5\%$, as shown in Section 4.2, Figure 4.4. As expected, the simulation with only radiative cooling is not converged in terms of condensation. However, with the inclusion of thermal conduction at $f = 0.1$ the condensation seems to be converged to a good degree at $\mathcal{R}_{32}$. We have not performed convergence tests for runs with other values of $f$. Since our run with $f = 0.1$ seems to evaporate the small scales that inhibit convergence for the only cooling run, we argue that our runs with even stronger thermal conduction with $f = 0.15$ and $f = 0.2$ are also converged. By the same argument, we expect that our runs with $f = 0.01$ and $f = 0.05$ are likely only marginally converged.

Magnetic fields can also suppress the formation of hydrodynamical instabilities (Sur et al., 2014). Grønnow et al. (2018) found that increasing the resolution for MHD simulations *decreases* the amount of condensation, which was attributed to the width of the wake being unresolved for lower resolution. Such wider wakes could make mixing more efficient. In this work, we do not see this effect. Instead, we find all resolutions predict a $\approx 20\%$ increase of cold gas after $1.6t_{cc}$. This thin wake effect could however be obfuscated since we have added turbulent velocities to the cloud.

Finally, considering that our resolution study seems to suggest convergence for runs including thermal conduction *or* a magnetic field, we might naively expect that it is likely that simulations including both thermal conduction *and* magnetic fields are also converged at $\mathcal{R}_{32}$. However, the effects of anisotropic thermal conduction could affect the results differently. For this setup we have run the $\mathcal{R}_{64}$ simulation to 12 Myrs ($\approx 0.4t_{cc}$), after which it was deemed computationally unfeasible. While 12 Myrs is too short to draw a reliable conclusion, we notice that the evolution is closest to that of the $\mathcal{R}_{32}$ run.
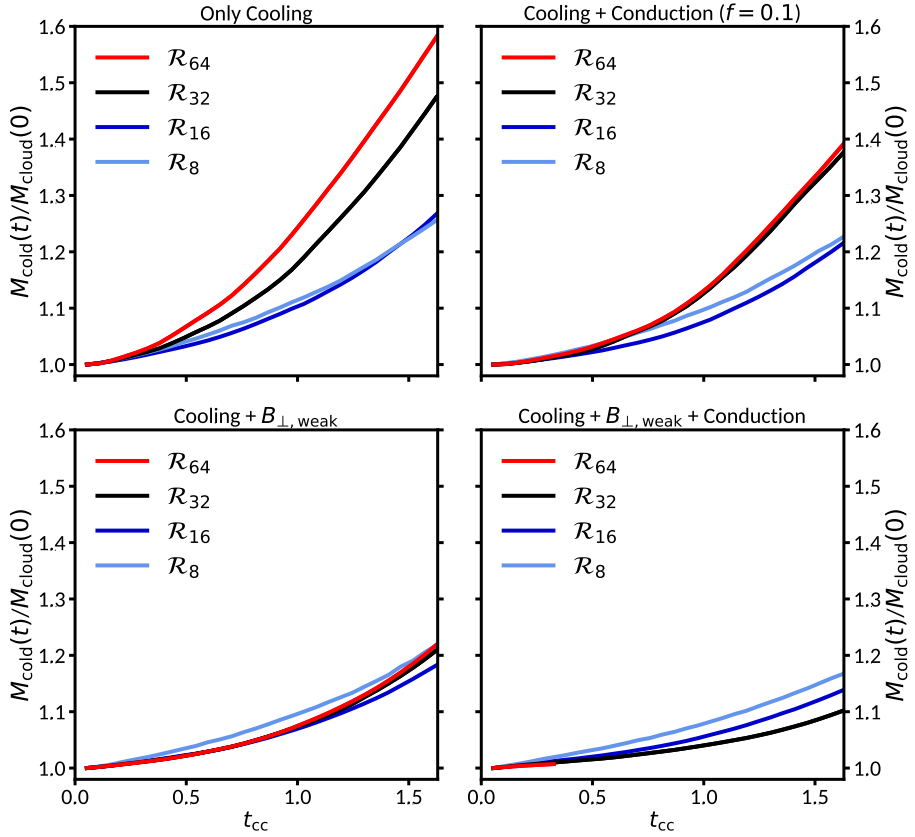
Figure 6.2: *Convergence tests in our primary diagnostic for our fiducial simulation setup for radiative cooling (top left), radiative cooling and conduction at $f = 0.1$ (top right), radiative cooling and a weak $(0.1 \mu G)$ perpendicular magnetic field with (right) and without (left) thermal conduction (bottom plots).*
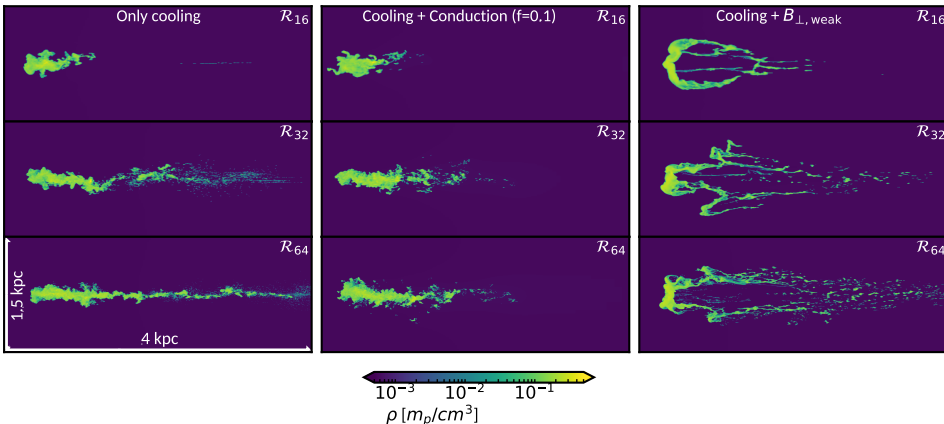
*Figure 6.3: Projected densities from the simulations for which convergence tests were performed. We show the only cooling runs on the left, the cooling and conduction at $f = 0.1$ in the middle, and cooling and a weak, perpendicular magnetic field on the right. From top to bottom we show low ($\mathcal{R}_{16}$), medium ($\mathcal{R}_{32}$), and high resolution ($\mathcal{R}_{64}$) runs, respectively. Note that we have not included the run with cooling, magnetic field, and conduction since the $\mathcal{R}_{64}$ run is incomplete.*

## 6.2 Limitations and Future Work

As mentioned in Section 5.5, the magnetic field of galaxies is expected to be tangled due to the ubiquitous sources of turbulence. However, simulating a tangled magnetic field was found to be problematic. A rapid untangling of the magnetic field was noticed, likely associated with the boundary conditions. It furthermore requires high resolution everywhere on the grid, and is computationally expensive since the timesteps become very small when anisotropic thermal conduction is included. We have tested this setup for $\sim 1t_{cc}$, and notice that similar to the perpendicular field, there is a draping effect around the cloud (but see also Asai et al., 2007). Hence, we expect the evolution of simulations with a tangled magnetic field to be roughly similar to the case of a perpendicular magnetic field. We leave the investigation of such systems to future work.

While our simulations contain the typically dominant physical processes: radiative cooling, thermal conduction and magnetic fields, we have not taken into account some physics. Most notably, we have not included self-gravity. Our cloud mass is $2.6 \times 10^4 \, M_\odot$, which is much less than the Jeans mass ($M_J \approx 1.6 \times 10^8 \, M_\odot$), so self-gravity is likely not important in this case. This conclusion is consistent with the findings of Li et al. (2019). Other physics not included in this work that were investigated by Li et al. (2019) are viscosity and self-shielding of cloud material, which are also likely not important for our cloud and halo parameters. Our cooling function assumes collisional ionisation equilibrium tables from Sutherland & Dopita (1993), which are slightly outdated. The collisional ionisation equilibrium assumes that the medium is optically thin for its own radiation, and that all ions are in their ground states (e.g. Dopita & Sutherland, 2003). These assumptions are very basic and in principle a chemical network based approach should be used to properly account for radiative cooling (see e.g. Salz et al., 2015). However, we do not expect significant changes to our results for different cooling functions. Furthermore, we implemented an artificial cooling floor to account for heating by a UV background. This prevents any gas from cooling to very low temperatures, but since we classify gas as cold when T $< 2 \times 10^4$ K the effect on the condensation will likely be small.

# Chapter 7

# Summary and conclusions

Fully 3D MHD simulations including anisotropic thermal conduction of "cloud-wind" systems have not been investigated thoroughly in the literature. In this work we presented such simulations for several magnetic field strengths, orientations and parameter setups. We furthermore presented 3D HD simulations with isotropic thermal conduction at a certain efficiency $f$. Our main goal was to compare the evolution of MHD simulations with anisotropic thermal conduction to HD simulations with isotropic thermal conduction at a certain $f$. We used the cold gas mass evolution as our primary diagnostic, and found that thermal conduction suppresses condensation in almost every case. For both HD and MHD simulations we isolated the effects of thermal conduction by dividing the cold gas mass evolution for runs with no thermal conduction to runs with thermal conduction, and directly compared the curves to find a suitable efficiency $f$.

We can draw the following conclusions:

1. In HD simulations, isotropic thermal conduction always suppresses condensation, where the suppression is stronger for more efficient thermal conduction (larger $f$). This was found to be primarily due to the evaporation of small, ablated cloudlets. Condensation was found to occur most prominently close to the galactic disc ($n_{\mathrm{hot}} = 10^{-3}$ cm$^{-3}$), and was found to be substantially smaller farther away from the galaxy ($n_{\mathrm{hot}} < 5 \times 10^{-4}$ cm$^{-3}$). Therefore, condensation is less efficient in the outer CGM.

2. In MHD simulations, anisotropic thermal conduction was found to suppress condensation more prominently for a magnetic field perpendicular to the relative velocity than for a parallel magnetic field. This was found to be due to the lack of ablated material in the parallel magnetic field setup as compared to perpendicular fields. The simulation with an oblique field produced very similar results to the perpendicular field setup, which showed that the perpendicular field setup is the most realistic.

3. Tangled magnetic fields are substantially more difficult to simulate due to computational constraints arising from very small timesteps. Additionally a decay of the magnetic field strength was spotted on relatively short timescales ($\approx 5$ Myrs). Regardless, the field remains mostly random, and was found to have a similar magnetic draping effect as the perpendicular magnetic field setup. It furthermore showed a similar effect on the suppression of condensation as the perpendicular field setup.

4. There is a dichotomy in efficiencies between parallel and transverse magnetic field orientations due to the distinct magnetic field interactions between the cloud and

the hot medium. Transverse fields were found to have a value of $f$ in the range $0.03 - 0.15$, whereas parallel fields have a value of $f$ in the range $0.01 - 0.06$. Since perpendicular fields have been found to be the most realistic field setup, an efficiency of $f$ in the range $0.03 - 0.15$ is likely most realistic.

Our resolution study shows that both thermal conduction and magnetic fields can aid in reaching convergence in terms of the total amount of cold gas formed as a function of time. This is a significant result: the shattering hypothesis (McCourt et al., 2018; Sparre et al., 2018; Liang & Remming, 2020) argues that thermal instability can shatter cold gas to very small scales. However, thermal conduction actively evaporates the smallest scales, which is why our run with thermal conduction appears to reach convergence.

We can conclude that *thermal conduction plays an important role in the CGM*. In almost all simulations thermal conduction was shown to reduce condensation. Since thermal conduction is highly temperature dependent ($F \propto T^{5/2}\nabla T$), we expect that its effect on the condensation will be greater for higher temperatures. This means that galaxies with a higher virial temperature ($T > 2 \times 10^6$ K), i.e. higher virial mass, likely experience less effective, or no fountain accretion.

While the approximation of a global efficiency of thermal conduction can in principle be used to simulate suppression due to magnetic fields, we urge caution. Magnetic fields have strong effects on cloud morphology, condensation, and in some cases the momentum transfer between cloud and halo. Therefore we stress that to obtain reliable estimates of accretion rates into galaxies and other properties linked to cloud-halo interactions in the CGM one must include magnetic fields and fully anisotropic thermal conduction.

# Acknowledgements

# Bibliography

Ahrens J., Geveci B., Law C., 2005, The visualization handbook, 717

Alfvén H., 1942, Nature, 150, 405

Anderson M. E., Bregman J. N., 2011, ApJ, 737, 22

Anderson M. E., Churazov E., Bregman J. N., 2016, MNRAS, 455, 227

Antonuccio-Delogu V., Silk J., 2010, MNRAS, 405, 1303

Armillotta L., Fraternali F., Marinacci F., 2016, MNRAS, 462, 4157

Armillotta L., Fraternali F., Werk J. K., Prochaska J. X., Marinacci F., 2017, MNRAS, 470, 114

Asai N., Fukuda N., Matsumoto R., 2007, ApJ, 663, 816–823

van Ballegooijen A. A., Cranmer S. R., 2010, ApJ, 711, 164

Banda-Barragán W. E., 2016, PhD thesis, Research School of Astronomy & Astrophysics, ANU

Banda-Barragán W. E., Federrath C., Crocker R. M., Bicknell G. V., 2018, MNRAS, 473, 3454

Banda-Barragán W. E., Federrath C., Crocker R. M., Bicknell G. V., 2017, MNRAS, 473, 3454–3489

Bauermeister A., Blitz L., Ma C.-P., 2010, ApJ, 717, 323

Beck R., 2003, arXiv e-prints, pp astro–ph/0310287

Beck R., 2009, Ap&SS, 320, 77

Beck R., 2015, A&ARv, 24, 4

Beck M. C., Beck A. M., Beck R., Dolag K., Strong A. W., Nielaba P., 2016, J. Cosmology Astropart. Phys., 2016, 056

Begelman M. C., McKee C. F., 1990, ApJ, 358, 375

Berkhuijsen E. M., Brouw W. N., 1963, Bull. Astron. Inst. Netherlands, 17, 185

Betti S. K., Hill A. S., Mao S. A., Gaensler B. M., Lockman F. J., McClure-Griffiths N. M., Benjamin R. A., 2019, ApJ, 871, 215

Birnboim Y., Dekel A., 2003, MNRAS, 345, 349

Bogdán Á., et al., 2012, ApJ, 755, 25

Brackbill J. U., Barnes D. C., 1980, J. of Comput. Phys., 35, 426

Braginskii S. I., 1965, Reviews of Plasma Physics, 1, 205

Braun R., Burton W. B., 2000, A&A, 354, 853

Bregman J. N., 1980, ApJ, 236, 577

Bregman J. N., 2007, ARA&A, 45, 221

Bregman J. N., Anderson M. E., Miller M. J., Hodges-Kluck E., Dai X., Li J.-T., Li Y., Qu Z., 2018, ApJ, 862, 3

Brent R. P., 1971, Comput. J., 14, 422

Brown R. H., Hazard C., 1951, MNRAS, 111, 357

Brown J. C., Haverkorn M., Gaensler B. M., Taylor A. R., Bizunok N. S., McClure-Griffiths N. M., Dickey J. M., Green A. J., 2007, ApJ, 663, 258

Brüns C., Kerp J., Kalberla P. M. W., Mebold U., 2000, A&A, 357, 120

Brüggen M., Scannapieco E., 2016, ApJ, 822, 31

Chandran B. D. G., Cowley S. C., 1998, Phys. Rev. Lett., 80, 3077

Chandrasekhar S., 1961, Hydrodynamic and hydromagnetic stability

Childs H., et al., 2012, in , High Performance Visualization–Enabling Extreme-Scale Scientific Insight. pp 357–372

Cooper J. L., Bicknell G. V., Sutherland R. S., Bland-Hawthorn J., 2009, ApJ, 703, 330

Cottle J., Scannapieco E., Brüggen M., Banda-Barragán W., Federrath C., 2020, ApJ, 892, 59

Courant R., Friedrichs K., Lewy H., 1928, Math. Ann., 100, 32

Cowie L. L., McKee C. F., 1977, ApJ, 211, 135

Crighton N. H. M., Hennawi J. F., Prochaska J. X., 2013, ApJ, 776, L18

Crighton N. H. M., Hennawi J. F., Simcoe R. A., Cooksey K. L., Murphy M. T., Fumagalli M., Prochaska J. X., Shanks T., 2015, MNRAS, 446, 18

Dai X., Anderson M. E., Bregman J. N., Miller J. M., 2012, ApJ, 755, 107

Dedner A., Kemm F., Kröner D., Munz C.-D., Schnitzer T., Wesenberg M., 2002, J. Comput. Phys., 175, 645

Dopita M. A., Sutherland R. S., 2003, Collisional Ionization Equilibrium. Springer Berlin Heidelberg, Berlin, Heidelberg, pp 101–123, doi:10.1007/978-3-662-05866-4_5, https://doi.org/10.1007/978-3-662-05866-4_5

Drazin P. G., 2002, Introduction to Hydrodynamic Stability

Drazin P. G., Reid W. H., 2004, Hydrodynamic Stability

Dursi L. J., Pfrommer C., 2008, ApJ, 677, 993

Einfeldt B., 1988, SIAM Journal on Numerical Analysis, 25, 294

Ekers R. D., Sancisi R., 1977, A&A, 54, 973

Faridani S., Flöer L., Kerp J., Westmeier T., 2014, A&A, 563, A99

Field G. B., 1965, ApJ, 142, 531

Fielding D., Quataert E., McCourt M., Thompson T. A., 2017, MNRAS, 466, 3810

Forman W., Schwarz J., Jones C., Liller W., Fabian A. C., 1979, ApJ, 234, L27

Forman W., Jones C., Tucker W., 1985, ApJ, 293, 102

Fraternali F., 2017, Ap&SS, p. 323–353

Fraternali F., Binney J. J., 2006, MNRAS, 366, 449

Fraternali F., Binney J. J., 2008, MNRAS, 386, 935

Fraternali F., Marasco A., Marinacci F., Binney J., 2013, ApJ, 764, L21

Fraternali F., Marasco A., Armillotta L., Marinacci F., 2015, MNRAS, 447, L70

Fukugita M., Peebles P. J. E., 2006, ApJ, 639, 590

Fukui Y., et al., 2018, PASJ

Fumagalli M., Hennawi J. F., Prochaska J. X., Kasen D., Dekel A., Ceverino D., Primack J., 2014, ApJ, 780, 74

Gatto A., Fraternali F., Read J. I., Marinacci F., Lux H., Walch S., 2013, MNRAS, 433, 2749

Godunov S. K., 1954, PhD thesis, Moscow State University

Godunov S. K., 1959, Mat. Sb. (N.S.), 47(89), 271

Goldsmith K. J. A., Pittard J. M., 2017, MNRAS, 470, 2427

Grcevich J., Putman M. E., 2009, ApJ, 696, 385

Grønnow A. E., 2018, PhD thesis, University of Sydney

Grønnow A., Tepper-García T., Bland-Hawthorn J., McClure-Griffiths N. M., 2017, ApJ, 845, 69

Grønnow A., Tepper-García T., Bland-Hawthorn J., 2018, ApJ, 865, 64

Haffner L. M., Reynolds R. J., Tufte S. L., Madsen G. J., Jaehnig K. P., Percival J. W., 2003, ApJS, 149, 405

Harten A., Lax P. D., Leer B. v., 1983, SIAM Review, 25, 35

Haverkorn M., Brown J. C., Gaensler B. M., McClure-Griffiths N. M., 2008, ApJ, 680, 362

Helmholtz P., 1868, London, Edinburgh Dublin Philos. Mag. J. Sci., 36, 337

Hennawi J. F., Prochaska J. X., Cantalupo S., Arrigoni-Battaia F., 2015, Science, 348, 779

Hernandez A. K., Wakker B. P., Benjamin R. A., French D., Kerp J., Lockman F. J., O'Toole S., Winkel B., 2013, ApJ, 777, 19

Hodges-Kluck E., Bregman J. N., 2014, ApJ, 789, 131

Houck J. C., Bregman J. N., 1990, ApJ, 352, 506

Humphrey P. J., Buote D. A., Canizares C. R., Fabian A. C., Miller J. M., 2011, ApJ, 729, 53

Hunter J. D., 2007, Comput. Sci. Eng., 9, 90

Irwin J., et al., 2012, AJ, 144, 44

Jansson R., Farrar G. R., 2012, ApJ, 757, 14

Jansson R., Farrar G. R., Waelkens A. H., Enßlin T. A., 2009, J. Cosmology Astropart. Phys., 2009, 021

Jiang G.-S., Wu C.-c., 1999, J. of Comput. Phys., 150, 561

Jones T. W., Ryu D., Tregillis I. L., 1996, ApJ, 473, 365

Kelvin S., 1871, London, Edinburgh Dublin Philos. Mag. J. Sci., 42, 362

Klein R. I., McKee C. F., Colella P., 1994, ApJ, 420, 213

Klessen R. S., Hennebelle P., 2010, A&A, 520, A17

Komatsu E., et al., 2009, ApJS, 180, 330

Komatsu E., et al., 2011, ApJS, 192, 18

Krause M., 2009, in Revista Mexicana de Astronomia y Astrofisica Conference Series. pp 25–29 (arXiv:0806.2060)

Krause G., 2019, A&A, 631, A68

Lau M. W., Prochaska J. X., Hennawi J. F., 2016, ApJS, 226, 25

Lax P. D., 1957, Commun. Pure Appl. Math., 10, 537

Lax P., Wendroff B., 1960, Commun. Pure Appl. Math., 13, 217

van Leer B., 1977, J. Comput. Phys., 23, 276

van Leer B., 1979, J. Comput. Phys., 32, 101

Lehner N., Howk J. C., Wakker B. P., 2015, ApJ, 804, 79

Li M., Bryan G. L., Ostriker J. P., 2017, ApJ, 841, 101

Li Z., Hopkins P. F., Squire J., Hummels C., 2019, MNRAS, p. 3180

Liang C. J., Remming I., 2020, MNRAS, 491, 5056

Mac Low M.-M., Klessen R. S., 2004, Rev. Mod. Phys., 76, 125

Mac Low M.-M., McCray R., Norman M. L., 1989, ApJ, 337, 141

Mac Low M.-M., McKee C. F., Klein R. I., Stone J. M., Norman M. L., 1994, ApJ, 433, 757

Marasco A., Fraternali F., Binney J. J., 2012, MNRAS, 419, 1107

Marasco A., Marinacci F., Fraternali F., 2013, MNRAS, 433, 1634

Marinacci F., 2011, PhD thesis, University of Bologna

Marinacci F., Binney J., Fraternali F., Nipoti C., Ciotti L., Londrillo P., 2010, MNRAS, 404, 1464

Marinacci F., Fraternali F., Nipoti C., Binney J., Ciotti L., Londrillo P., 2011, MNRAS, 415, 1534

Martin C. L., 1999, ApJ, 513, 156

McCourt M., O'Leary R. M., Madigan A.-M., Quataert E., 2015, MNRAS, 449, 2

McCourt M., Oh S. P., O'Leary R., Madigan A.-M., 2018, MNRAS, 473, 5407

Mignone A., Bodo G., Massaglia S., Matsakos T., Tesileanu O., Zanni C., Ferrari A., 2007, ApJS, 170, 228

Mignone A., Tzeferacos P., Bodo G., 2010, J. Comput. Phys., 229, 5896

Mignone A., Zanni C., Tzeferacos P., van Straalen B., Colella P., Bodo G., 2011, ApJS, 198, 7

Miller M. J., Bregman J. N., 2013, ApJ, 770, 118

Miyoshi T., Kusano K., 2005, J. Comput. Phys., 208, 315

Muller C. A., Oort J. H., Raimond E., 1963, C. R. Acad. Sci, 257, 1661

Narayan R., Medvedev M. V., 2001, ApJ, 562, L129

Oliphant T., 2006, NumPy: A guide to NumPy, USA: Trelgol Publishing, http://www.numpy.org/

Oosterloo T., Fraternali F., Sancisi R., 2007, AJ, 134, 1019

Pezzulli G., Fraternali F., 2016, MNRAS, 455, 2308

Prochaska J. X., Hennawi J. F., 2008, ApJ, 690, 1558

Putman M. E., Saul D. R., Mets E., 2011, MNRAS, 418, 1575

Putman M. E., Peek J. E. G., Joung M. R., 2012, ARA&A, 50, 491

Qu Z., Bregman J. N., Hodges-Kluck E. J., 2019, ApJ, 876, 101

Rayleigh 1882, P. Lond. Math. Soc., s1-14, 170

Richings A. J., Schaye J., Oppenheimer B. D., 2014, MNRAS, 440, 3349

Richter P., Sembach K. R., Wakker B. P., Savage B. D., Tripp T. M., Murphy E. M., Kalberla P. M. W., Jenkins E. B., 2001, ApJ, 559, 318

Richter P., et al., 2017, A&A, 607, A48

Roe P. L., 1981, J. Comput. Phys., 43, 357

van Rossum G., Drake F. L., 2009, Python 3 Reference Manual. CreateSpace, Scotts Valley, CA

Salz M., Banerjee R., Mignone A., Schneider P. C., Czesla S., Schmitt J. H. M. M., 2015, A&A, 576, A21

Sancisi R., Allen R. J., 1979, A&A, 74, 73

Schaal K., Bauer A., Chandrashekar P., Pakmor R., Klingenberg C., Springel V., 2015, MNRAS, 453, 4278

Sembach K. R., et al., 2003, ApJS, 146, 165

Shapiro P. R., Field G. B., 1976, ApJ, 205, 762

Shu C.-W., 1998, Essentially non-oscillatory and weighted essentially non-oscillatory schemes for hyperbolic conservation laws. Springer

Shu C.-W., 2009, SIAM review, 51, 82

Sod G. A., 1978, J. Comput. Phys., 27, 1

Sparre M., Pfrommer C., Vogelsberger M., 2018, MNRAS, 482, 5401

Spitoni E., Recchi S., Matteucci F., 2008, A&A, 484, 743

Spitzer Lyman J., 1956, ApJ, 124, 20

Spitzer L., 1962, Physics of Fully Ionized Gases

Stocke J. T., Keeney B. A., Danforth C. W., Shull J. M., Froning C. S., Green J. C., Penton S. V., Savage B. D., 2013, ApJ, 763, 148

Stone J. M., Gardiner T., 2007, Physics of Fluids, 19, 094104

Stone J. M., Gardiner T. A., Teuben P., Hawley J. F., Simon J. B., 2008, ApJS, 178, 137

Sur S., Pan L., Scannapieco E., 2014, ApJ, 784, 94

Sutherland R. S., Dopita M. A., 1993, ApJS, 88, 253

Taylor G., 1950, P. Lond. Math. Soc. Series A, 201, 192

Tepper-García T., Bland-Hawthorn J., Pawlowski M. S., Fritz T. K., 2019, MNRAS, 488, 918

Toro E. F., Spruce M., Speares W., 1994, Shock Waves, 4, 25

Tufte S. L., Reynolds R. J., Haffner L. M., 1998, ApJ, 504, 773

Tumlinson J., et al., 2011, Science, 334, 948

Tumlinson J., Peeples M. S., Werk J. K., 2017, ARA&A, 55, 389

Turk M. J., Smith B. D., Oishi J. S., Skory S., Skillman S. W., Abel T., Norman M. L., 2010, ApJS, 192, 9

Vieser W., Hensler G., 2007, A&A, 472, 141

Vietri M., Ferrara A., Miniati F., 1997, ApJ, 483, 262

van de Voort F., Schaye J., Altay G., Theuns T., 2012, MNRAS, 421, 2809

Wadsley J. W., Keller B. W., Quinn T. R., 2017, MNRAS, 471, 2357

Wakker B. P., 2001, ApJS, 136, 463–535

Wakker B. P., van Woerden H., 1991, A&A, 250, 509

Wakker B. P., van Woerden H., 1997, ARA&A, 35, 217

Wakker B. P., et al., 2007, ApJ, 670, L113

Weinberger R., Springel V., Pakmor R., 2020, ApJS, 248, 32

Werk J. K., Prochaska J. X., Thom C., Tumlinson J., Tripp T. M., O'Meara J. M., Peeples M. S., 2013, ApJS, 204, 17

Werk J. K., et al., 2014, ApJ, 792, 8

Werk J. K., et al., 2016, ApJ, 833, 54

Westerhout G., Seeger C. L., Brouw W. N., Tinbergen J., 1962, Bull. Astron. Inst. Netherlands, 16, 187

White S. D. M., Frenk C. S., 1991, ApJ, 379, 52

White S. D. M., Rees M. J., 1978, MNRAS, 183, 341

Wielebinski R., Shakeshaft J. R., 1962, Nature, 195, 982

Xu J., Stone J. M., 1995, ApJ, 454, 172

Yamasaki N. Y., Sato K., Mitsuishi I., Ohashi T., 2009, PASJ, 61, S291

Zheng Y., Peek J. E. G., Werk J. K., Putman M. E., 2017, ApJ, 834, 179